

Emitter-Optomechanical Interaction in high-Q hBN Nanocavities

Chenjiang Qian,^{1,*} Viviana Villafaña,¹ Martin Schalk,¹ Georgy V. Astakhov,² Ulrich Kentsch,² Manfred Helm,² Alexander Hötger,¹ Pedro Soubelet,¹ Alexander W. Holleitner,¹ Andreas V. Stier,¹ and Jonathan J. Finley^{1,†}

¹Walter Schottky Institut and Physik Department,

Technische Universität München, Am Coulombwall 4, 85748 Garching, Germany

²Helmholtz-Zentrum Dresden-Rossendorf, Institute of Ion Beam Physics and Materials Research, 01328 Dresden, Germany

We investigate the interaction between charged boron vacancies V_B^- in hBN and optomechanical modes in a nanobeam cavity using spatially resolved photoluminescence (PL) and Raman spectroscopy. V_B^- is a point defect emitter and the emission is dominated by phonon-assisted processes. As such, the V_B^- emission is intrinsically sensitive to, and interacts with local deformations such as lattice phonons and cavity optomechanical vibrations. We observe a pronounced spectral asymmetry of the high-Q ($\sim 10^5$) nanocavity photonic mode that is only presented for cavities containing V_B^- emitters, revealing the emitter-induced active cavity optomechanics. Meanwhile, we reveal the cavity-induced control of phonon-assisted V_B^- emission by exploring the luminescence with position-dependent vibrations in freely suspended structures and the resonant excitation of cavity photons with cooling and heating detunings. Our results show how V_B^- defect related phonons mediate the coupling between defect emission, cavity photonic and vibronic modes as an emitter-optomechanical system. Such an interplay between different vibronic (defect phonon, nanomechanical vibration) and photonic (cavity modes) extends the cavity QED system and provide new paradigms for interfacing spin, photons and phonons in condensed matters.

Hexagonal boron nitride (hBN) is a wide bandgap 2D semiconductor that has recently been found to host a variety of point defects of interest for single photon generation, spin-photon interfaces and quantum sensing [1–6]. The negatively charged boron vacancy V_B^- is attracting particular interest due to its paramagnetic nature and spin-dependent optical properties at room temperature [4–8]. V_B^- emission is dominated by phonon sidebands, indicative of strong electron-phonon coupling during radiative recombination [9–12]. In addition, hBN has high thermal and chemical stability, and can be readily integrated into high-Q nanophotonic structures [12–15]. The electronic and optical properties of hBN are sensitive to local deformations caused e.g. by bending or dynamical strain arising from the phononic vibration of nanophotonic structures [16–20]. Therefore, by creating V_B^- defects in an hBN nanocavity that supports localized photonic and vibronic modes [21–23], we realize an emitter-optomechanical system in which defect phonons mediate couplings between defect emissions, cavity photons and cavity vibrations.

Here we investigate the emitter-optomechanical interaction in the cavity- V_B^- system using spatially resolved photoluminescence (PL) and Raman spectroscopy. We observe a pronounced spectral asymmetry of the high-Q ($\sim 10^5$) nanocavity photonic mode that is only present for nanobeam cavities in which V_B^- defects have been created via N^+ ion irradiation [12, 24, 25]. We show that the asymmetry arises from an optical bistability involving cavity photons during the photon-phonon coupling [26–28]. This asymmetry is not observed for non-irradiated cavities, indicating that the phonons involved in the photon-phonon coupling are not thermally excited but rather generated during the emission of V_B^- [9–12].

We establish the interaction between cavity optomechanical modes and phonon-assisted V_B^- emissions by spatially correlating luminescence with position-dependent vibronic modes in freely suspended structures [20] and the resonant excitation of cavity photons [26]. Through the position dependence we find that out-of-plane vibrations generally enhance and red shift the V_B^- emission whilst in-plane vibrations do the opposite. In the resonant excitation, the Raman signals of V_B^- phonons exhibit a significant and asymmetric enhancement at the cooling and heating detunings [26] as a direct evidence for the cavity vibration mediated coupling between cavity photons and V_B^- phonons. As the out-of-plane vibration amplitude further increases, an eight fold enhancement of PL intensity [20] and anticrossings between replica peaks [29] are observed. These results demonstrate the strong interplay between multiple degrees of freedom in the emitter-optomechanical interaction. Such multi-modal couplings provide new paradigms for tailoring the interface between spin defects, photons and phonons in condensed matters [30].

The structure of our hybrid hBN/Si₃N₄ nanocavity is schematically depicted in Fig. 1. Detailed fabrication procedures for the samples have been reported in our previous work [12, 15] and also presented in supplemental material. The confinement of cavity photons is achieved by locally chirping the photonic crystal periodicity to create high-Q quasi 0D photonic modes. Besides discrete photonic modes, the cavity also supports vibronic modes since the nanobeam is freely suspended, but clamped at both edges [21–23]. Both photonic and vibronic modes are depicted schematically in Fig. 1. In Sample-A, selected hBN nanobeam cavities were irradiated by 30 kV N^+ ions with a dose of 10^{13} ions/cm² to create boron va-

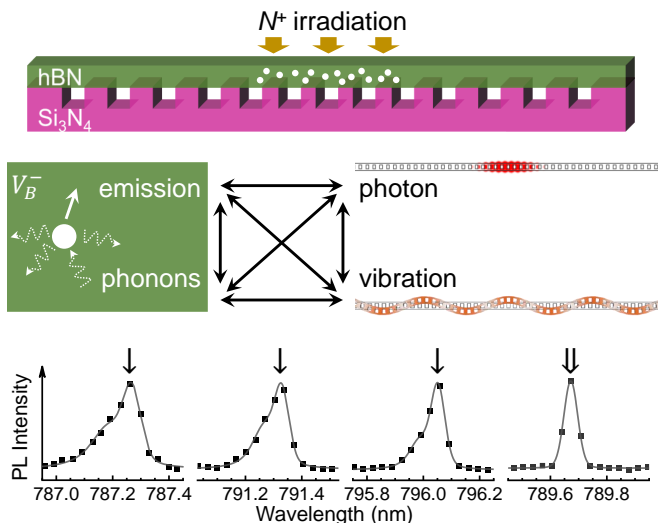


FIG. 1. Schematic of cavity structure and irradiated region for Sample-A. The V_B^- emission is dominated by phonon sidebands. The cavity supports photonic and vibronic modes. Thereby, the system involves the multipartite interplay between V_B^- emission, localized phonons associated with V_B^- , cavity photons and cavity vibrations. Typical emission spectra of the cavity photonic modes from N^+ irradiated samples (labelled \downarrow) and non-irradiated cavities (labelled \Downarrow). As discussed in the text, the irradiated cavities exhibit a clear asymmetric line shape, revealing the optical bistability arising from photon-phonon coupling. In contrast, no asymmetry in the lineshape is observed when the hBN is not irradiated.

cancies within the volume of photonic mode [12, 24, 25]. V_B^- exhibits bright emission at room temperature [5, 6] dominated by phonon sidebands [9–12], whilst the zero-phonon line ~ 773 nm [12] is weak. Compared to emitters dominated by zero-phonon emission such as TMD excitons, electron-phonon coupling in the V_B^- center is intrinsically strong, even at low temperature [5]. This gives rise to a spectrally broad emission, and the cavity vibronic mode is expected to play an important role in the V_B^- emission. The cavity- V_B^- system involves coupling between defect emission, defect phonons, cavity photons and cavity vibrations, as an emitter-optomechanical system depicted schematically in Fig. 1.

We begin by comparing the spectral form of the emission observed from the cavities with and without N^+ irradiation. Sample-A is excited using a 532nm cw-laser having a spot size ~ 1 μm and the power ~ 120 μW . The cavity photonic mode is thereby excited by the created V_B^- centers and/or some native defects in the hBN and underlying Si_3N_4 . All cavities exhibit high Q values $\geq 10^4$, limited only by the spectral resolution of our detection system [15]. Furthermore, for N^+ irradiated cavities we observe a strongly asymmetric lineshape of cavity photons that is broadened on the short wavelength (high energy) side. Typical data are presented in Fig. 1 and all irradiated (non-irradiated)

cavities exhibit similar results. We identify the asymmetric peak as arising from optical bistability, a well-known nonlinear optomechanical phenomenon originating from the strong photon-phonon coupling [26–28]. Without the phonons, the spectral density of cavity photons is well described by a Lorentzian lineshape, $D_C(\omega) = (\gamma_C/2\pi)/[(\omega - \omega_C)^2 + (\gamma_C/2)^2]$, where ω_C and γ_C are the energy and decay rate of the cavity photon, a spectral function that is evidently symmetric [31]. However, the photon-phonon coupling red shifts the optical resonance by an amount $8g_p^2 N(\omega)/\omega_p$ proportional to the photon number $N(\omega)$ [26]. ω_p is the typical phonon energy and g_p is the photon-phonon coupling strength per photon. Since $N(\omega) \propto D_C(\omega)$ varies with ω , the non-uniform energy shift is expected to result in an asymmetric peak in the spectrum, precisely as observed in Fig. 1. Moreover, we do not observe any asymmetry in any of our control experiments for which the hBN was not irradiated with N^+ . This is one of the central results of this paper, revealing that the phonons involved in the photon-phonon coupling are not thermally excited but generated during the emission of V_B^- centers. As expected, the asymmetry in the peak lineshape becomes stronger with increasing laser power (see supplemental material), due to the enhanced photon-phonon coupling arising from the increasing population of photons and phonons [27, 28].

The novel V_B^- -induced optomechanics presented in the context of Fig. 1 reveal that V_B^- phonons play a central role in the coupling dynamics of the system. Generally, two phonon processes exist in the emission of 0D emitters when non-resonantly excited, as schematically depicted in Fig. 2(a). The blue dashed arrow involves creating the negatively charged state by trapping a laser-excited electron [33, 34]. After the V_B^- state has been excited, coupling between the trapped electron and localized phonons (red dashed arrows in Fig. 2(a)) gives rise to the replicas and phonon sidebands in the emission spectrum. Since V_B^- emission is dominated by the phonon sidebands [9–12], the wavelengths of emission peaks are determined by the dominant phonon energies in the replica process. Considering the electron-phonon overlap [35, 36] depicted schematically in Fig. 2(a), one may expect that extended phonons which involve the vibration of multiple atoms (blue rings) govern the trapping process, whilst more strongly localized phonons involving only the vibrations of neighboring atoms (red rings) dominate the replica process. J. Li et al. [32] recently reported Raman spectroscopy of V_B^- defects, and unveiled this picture of Raman peaks for highly localized and extended phonons via the boron isotope characterization.

To confirm this picture of V_B^- emission in Fig. 2(a) and the interaction with vibronic modes in nanophotonic structures, we recorded PL and Raman spectroscopy from a second sample (Sample-B) that was homogeneously irradiated by N^+ ions at 30 kV voltage and a dose of 10^{14} ions/cm² [12, 24, 25] as shown in Fig. 2(b).

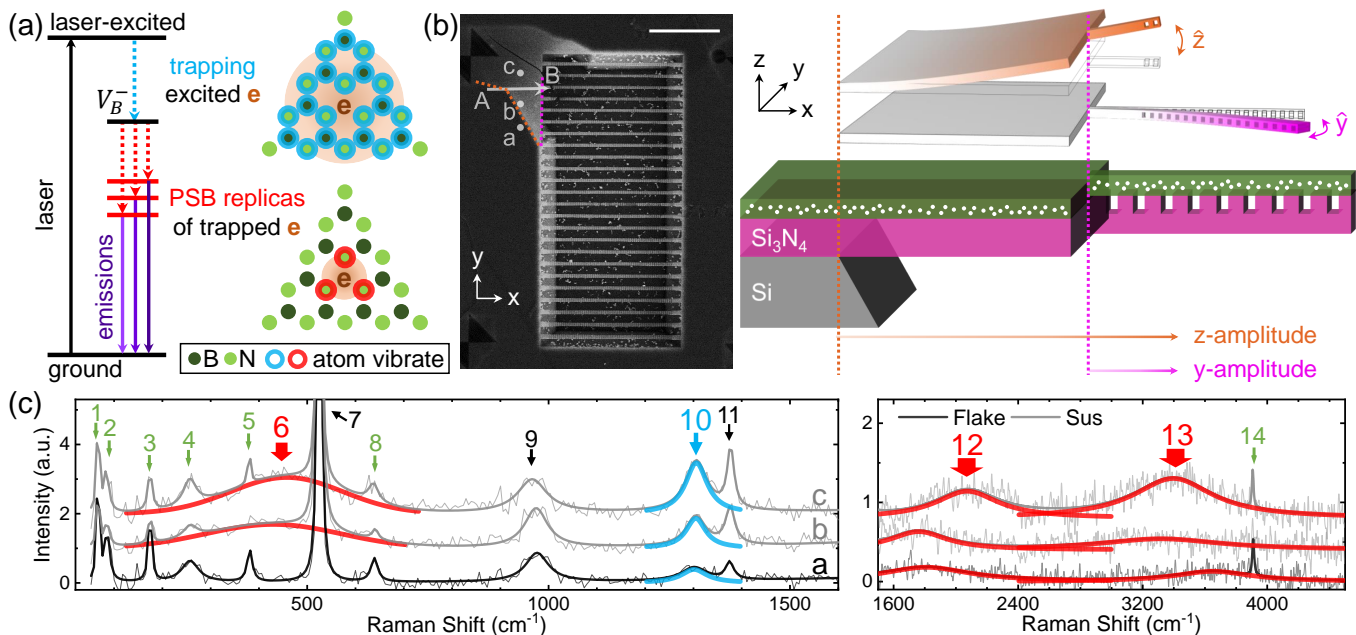


FIG. 2. (a) Schematic representation of the V_B^- excitation, thermalization and emission processes: Due to the spatial overlap between the electron wavefunction (schematically depicted by the brown shaded region) and the atoms involved in the local phonon modes (blue/red rings), the extended phonons from the defect complex (blue rings) are expected to dominate the trapping process (blue dashed arrow), and the localized phonons (red rings) dominate the replica processes (red dashed arrows). (b) SEM image of Sample-B, including the large region of unpatterned suspended membrane (upper left) and an array of nanobeam cavities in middle. The white scale bar is 10 μm . The sample structure and the corresponding vibronic modes are schematically depicted in the upper right. (c) Typical position-dependent Raman spectra recorded from positions *a*, *b* and *c* shown on (b). Phonon modes r1-14 are observed in the supported flake (black) and two suspended positions (gray). Peak r10 (blue) is the extended phonon [32]. Broad peaks r6,12,13 (red) are localized phonons [32] and are the only ones exhibiting distinguishable energy shift in this work. Other peaks exhibit few direct relation to the V_B^- emission.

Sample-B contains three different regions of interest: (i) the non-underetched region with hBN on planar $\text{Si}_3\text{N}_4/\text{Si}$ substrate corresponding to the dark surrounding region in the SEM image, (ii) the large suspended membrane of hBN/ Si_3N_4 layers suspended on etched Si corresponding to the large bright regions at left top, and (iii) suspended cavities with a varying nanobeam width d_y . No photonic modes exist in the large suspended membrane or the edge of nanobeams. Instead, as depicted schematically in Fig. 2(b), the system has vibronic modes with amplitudes determined by the position relative to the clamping points. These vibronic modes have characteristic frequencies in the range around 10 to 200 MHz [23]. As shown in Fig. 2(b), the large suspended membrane and the nanobeam both support out-of-plane *z*-vibrations, and the nanobeam additionally supports in-plane *y*-vibrations. Therefore, the optomechanical interactions with the V_B^- emission through in- and out-of-plane vibronic modes can be separated by comparison the PL and Raman spectra recorded spatially resolved from these different regions.

Typical representative Raman spectra measured from position (labelled *a*) on the non-underetched region and two different positions (labelled *b* and *c*) in the large sus-

pended membrane are presented in Fig. 2(c). Various Raman peaks are observed and labelled r1-14 on the figure. Peaks r7 at 524 cm^{-1} and r9 around 975 cm^{-1} are the bulk Si phonons [37], and r11 at 1377 cm^{-1} is the bulk hBN phonon E_{2g} [32]. The other peaks are not observed in Si_3N_4 nor non-irradiated hBN (see supplemental material), therefore identified as arising from V_B^- defects. Peaks r6 around 450 cm^{-1} (red) and r10 at 1306 cm^{-1} (blue) have been previously identified: r6 is the highly localized phonon and r10 is the extended phonon [32] discussed in the context of Fig. 2(a). We observe two other broad Raman features with higher energies: r12 around 1800 cm^{-1} (quadruple of r6), and r13 around 3600 cm^{-1} (double of r12). The broader Raman linewidth typically implies the stronger spatial confinement of the phonon mode [38–40]. In addition, r6,12,13 are the only V_B^- phonons exhibiting distinguishable energy shifts, e.g., between three positions in Fig. 2(c). These common features indicate that r12,13 are from multi-phonon states of r6 and also highly localized at the V_B^- defect. The other Raman peaks r1-5,8,14 at $67, 86, 174, 256, 382, 638, 3909 \text{ cm}^{-1}$ exhibit little energy shift between different detection positions, and their intensity variation do not follow the intensity of V_B^- emis-

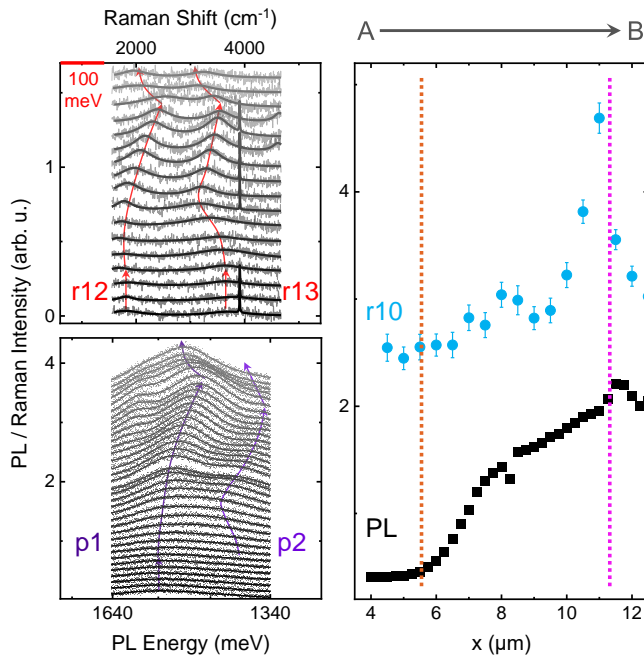


FIG. 3. (up) Raman and (bottom) PL spectra measured from from positions along the contour A-B in Fig. 2(b). (right) The corresponding intensity of extended phonon r10 and total PL emission. The orange and magenta dashed lines correspond to the boundaries in Fig. 2(b).

sions. Thus, we do not discuss these features here but rather in the supplemental material.

Raman and PL spectra measured from positions along the contour labelled A-B in Fig. 2(b) are presented in Fig. 3. The contour includes three regions as the non-underetched region, large suspended membrane and nanobeam cavity. The energy shift of the localized phonons and PL peaks in the three regions are denoted by the three-stage arrows in the up and bottom panels, respectively. The position-dependent energy shift of phonon r12,13 nicely track the shifts of the PL peaks p1,2, revealing that p1,2 are phonon sidebands arising from the localized phonons r12,13. Meanwhile, independent of whether PL emission arises from one phonon replica or the other, the total PL intensity is determined by the activated emitters through the trapping process. The variation of the local spectrally integrated PL intensity generally tracks the intensity variation of phonon r10 (right panel in Fig. 3). A similar correspondence between Raman and PL intensities has been observed for nitrogen vacancies in hBN [41], further supporting that phonon r10 is involved in the excitation of V_B^- . These two correlations between Raman and PL spectra in Fig. 3 agree well to the two predicted phonon processes in the V_B^- emission in Fig. 2(a).

Moreover, as previously discussed in the context of Fig. 2(b), the large suspended membrane and the nanobeam both support modes for which out-of-plane (z-

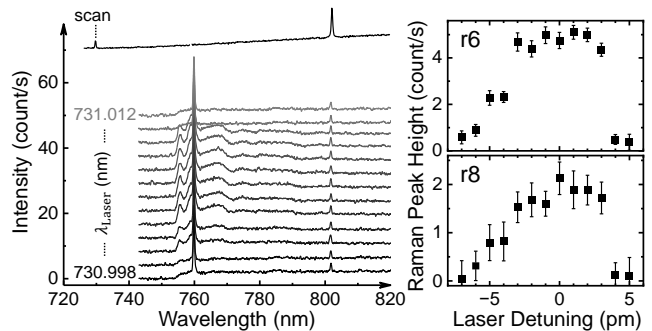


FIG. 4. Resonant excitation of a cavity photonic mode. The enhancement of V_B^- phonons r6,8 reveals the coupling between cavity photons and V_B^- phonons. The asymmetric enhancement at cooling and heating detunings indicates this coupling mediated by the cavity vibrations. Inset black line is the PL spectrum excited by 532nm laser with the scanned mode denoted. The peak at 802 nm is from another cavity photonic mode and has little impact on the resonance.

axis) vibration dominates, and the nanobeam in addition supports modes with in-plane (y-axis) character. Therefore, the emitter-optomechanical interaction effects with in- and out-of-plane vibronic modes can be separated by focusing our measurements on between different regions of the sample. By comparing the position dependence, e.g. datasets in Fig. 3, we find that the out-of-plane vibration in large suspended membrane ($x = 5 - 11 \mu\text{m}$) enhances the total PL intensity and red shifts the PL peak p1. This is accompanied by corresponding effects on the V_B^- phonons including the enhanced r10 intensity and blue shift of r12. In contrast, the in-plane vibration in the nanobeam region ($x > 11 \mu\text{m}$) has the opposite effects, suppressing the total PL intensity and blue shifting the PL peak p1. These characteristic impacts of in- and out-of-plane vibronic modes on the V_B^- emission is further found to be consistent with results obtained on nanobeam cavities spanning the region between non-underetched regions of the structure (bottom cavities in Fig. 2(b)). In this case there is no large suspended membrane and the V_B^- emission is determined by the superposition of y- and z-polarized modes. The degree of superposition qualitatively depends on the nanobeam width d_y since the y-bending rigidity varies with d_y [42]. We note that other potential effects that may impact on the PL spectra, such as photon reflection and thin-film interference, can be excluded since no differences could be observed by tilting the sample. Detailed discussions on the superposition of y-/z- vibrations and excluding other possibilities can be found in supplemental material.

In Fig. 2 and 3, we study the emitter-optomechanical interaction by controlling the vibration through the position dependence in suspended structures [20]. We continue to explore the control of cavity photonic and vibronic modes via the resonant excitation. Typical results are presented in Fig. 4. The cavity photons at 731 nm are

excited by a narrow cw-laser with the wavelength tuned over the interval 730.998 to 731.012 nm. Meanwhile, the cavity vibrations are controlled by the cooling (heating) effect through the positive (negative) detuning [26]. As the resonant laser is tuned over the cavity resonance we observe a clear resonance in the Raman peaks associated with the V_B^- phonons r6,8. The amplitude of these two features are plotted in the rightmost part of Fig. 4. The $> 10\times$ enhancement reveals the significant coupling between cavity photons and V_B^- phonons. In comparison, only a $< 10\%$ enhancement of the Si_3N_4 phonon r7 is observed over the same detuning range (see supplemental material). We believe the coupling between cavity photons and V_B^- phonons is mediated by the cavity vibrations, since the enhancement of V_B^- phonons is weak when the cavity vibration is cooled (positive detuning) and strong at opposite side [26], as shown by the asymmetric form of the detuning dependent-enhancement in Fig. 4. In addition to the emitter-induced cavity optomechanics in Fig. 1, and the cavity-induced control of V_B^- emissions and phonons in Fig. 2 and 3, we conclude that the V_B^- emissions, V_B^- phonons, cavity photons, and cavity vibrations interact to each other, demonstrating the emitter-optomechanical interaction in our cavities.

Finally, we show that the emitter-optomechanical interaction reconstructs the phonon couplings to the V_B^- state. Hereby, we observed clear anticrossings between sub-structure forming the broad position-dependent PL and Raman spectra. Figure 5(a) shows a typical intensity map of phonon r10 and 5(b) is the comparable map of total PL intensity as the laser focal volume traces specific paths in the data. These two maps are similar since phonon r10 dominates the trapping process, as discussed in the context of Fig. 2. Indeed, the results in Fig. 3 are extracted from the trace ① in Fig. 5(a)(b). Compared to trace ①, the z-amplitude in trace ② is much larger since the positions are far away to the clamping point. As a result, the total PL intensity exhibits an eight-fold enhancement close to the position having the maximum z-amplitude, a maximum compared to the non-underetched region. The shift of localized phonons and PL peaks are presented in Fig. 5(c), and the good agreement is again observed except some minor differences due to the the trace ② in two maps are not perfectly same in spatial. Furthermore, the energy differences between peaks are non-monotonic and exhibit clear anticrossing features. To prove the anticrossing, we extracted the PL spectra in the closed loop trace ③ in Fig. 5(b) and present the peak shifts in Fig. 5(d). If the peaks simply shifted during the measurement without anticrossing, they would not shift back to their initial positions at the end of loop, which is an obvious contradiction. Only through two anticrossings denoted on the figure, the peaks can shift back after the loop. Similar anticrossings along the loop trace are observed in Raman spectra (see supplemental material), demonstrating the

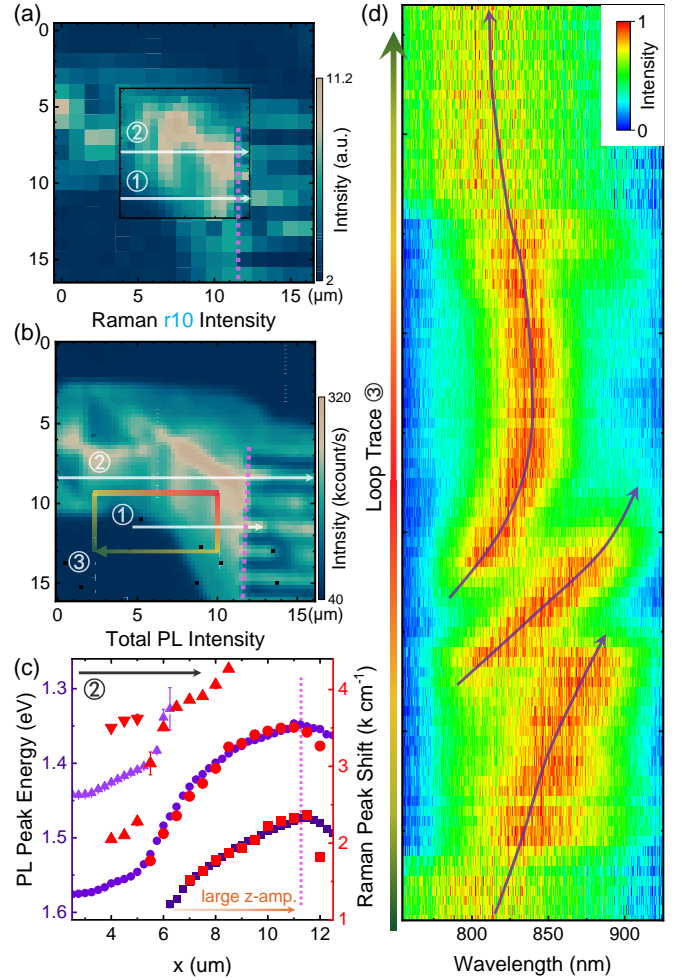


FIG. 5. The intensity map of (a) Raman peak r10 and (b) total PL emission. (c) Raman and PL peak energies extracted from trace ② in (a)(b). (d) Map of normalized PL spectra extracted from loop trace ③ in (b). Anticrossing is clearly demonstrated, otherwise the PL peak cannot shift back after the loop.

strong coupling between V_B^- phonon states induced by the vibrations [29].

In summary, we report the emitter-optomechanical interaction involving the multipartite interplay between the emission from defect centers, localized (defect) phonons, cavity photons and cavity nanomechanical vibrations in the cavity- V_B^- system. The PL and Raman spectroscopy demonstrate the emitter-induced cavity optomechanics and the cavity-induced control of phonon-assisted V_B^- emissions. For traditional emitters dominated by zero-phonon emission, their interaction to the cavity optomechanical modes is relative weak, e.g., the emission energy rarely shifts if without strong external mechanical drive [23, 43, 44]. In contrast, V_B^- is dominated by broad phonon sideband emission [9–12] thereby is also a phonon generator. The V_B^- phonons bridge the interaction between several degrees of freedom, resulting in the signifi-

cant emitter-optomechanical coupling phenomena in the system studied. Our work greatly extends the study of cavity QED and optomechanical systems by introducing the emitter-phonon degree of freedom, and we believe our results provide feasible approaches to the quantum interface between spin defects, photons and phonons.

All authors gratefully acknowledge the German Science Foundation (DFG) for financial support via grants FI 947/8-1, DI 2013/5-1 and SPP-2244, as well as the clusters of excellence MCQST (EXS-2111) and e-conversion (EXS-2089). A. W. H. and J. J. F. acknowledge the state of Bavaria via the One Munich Strategy and Munich Quantum Valley. C. Q. and V. V. gratefully acknowledge the Alexander v. Humboldt foundation for financial support in the framework of their fellowship programme. Support by the Ion Beam Center (IBC) at HZDR is gratefully acknowledged.

* chenjiang.qian@wsi.tum.de

† finley@wsi.tum.de

- [1] T. T. Tran, K. Bray, M. J. Ford, M. Toth, and I. Aharonovich, Quantum emission from hexagonal boron nitride monolayers, *Nat. Nanotechnol.* **11**, 37 (2016).
- [2] A. Sajid, M. J. Ford, and J. R. Reimers, Single-photon emitters in hexagonal boron nitride: a review of progress, *Rep. Prog. Phys.* **83**, 044501 (2020).
- [3] N. Mendelson, D. Chugh, J. R. Reimers, T. S. Cheng, A. Gottscholl, H. Long, C. J. Mellor, A. Zettl, V. Dyakonov, P. H. Beton, S. V. Novikov, C. Jagadish, H. H. Tan, M. J. Ford, M. Toth, C. Bradac, and I. Aharonovich, Identifying carbon as the source of visible single-photon emission from hexagonal boron nitride, *Nat. Mater.* **20**, 321 (2021).
- [4] H. L. Stern, Q. Gu, J. Jarman, S. Eizagirre Barker, N. Mendelson, D. Chugh, S. Schott, H. H. Tan, H. Siringhaus, I. Aharonovich, and M. Atatüre, Room-temperature optically detected magnetic resonance of single defects in hexagonal boron nitride, *Nat. Commun.* **13**, 618 (2022).
- [5] M. Kianinia, S. White, J. E. Fröch, C. Bradac, and I. Aharonovich, Engineering spin defects in hexagonal boron nitride (2020), [arXiv:2004.07968](https://arxiv.org/abs/2004.07968).
- [6] A. Gottscholl, M. Kianinia, V. Soltamov, S. Orlinkii, G. Mamin, C. Bradac, C. Kasper, K. Krambrock, A. Sperlich, M. Toth, I. Aharonovich, and V. Dyakonov, Initialization and read-out of intrinsic spin defects in a van der waals crystal at room temperature, *Nat. Mater.* **19**, 540 (2020).
- [7] A. Gottscholl, M. Diez, V. Soltamov, C. Kasper, D. Krauß, A. Sperlich, M. Kianinia, C. Bradac, I. Aharonovich, and V. Dyakonov, Spin defects in hbn as promising temperature, pressure and magnetic field quantum sensors, *Nat. Commun.* **12**, 4480 (2021).
- [8] W. Liu, Z.-P. Li, Y.-Z. Yang, S. Yu, Y. Meng, Z.-A. Wang, Z.-C. Li, N.-J. Guo, F.-F. Yan, Q. Li, J.-F. Wang, J.-S. Xu, Y.-T. Wang, J.-S. Tang, C.-F. Li, and G.-C. Guo, Temperature-dependent energy-level shifts of spin defects in hexagonal boron nitride, *ACS Photonics* **8**, 1889 (2021).
- [9] V. Ivády, G. Barcza, G. Thiering, S. Li, H. Hamdi, J.-P. Chou, Ö. Legeza, and A. Gali, Ab initio theory of the negatively charged boron vacancy qubit in hexagonal boron nitride, *npj Comput. Mater* **6**, 41 (2020).
- [10] J. R. Reimers, J. Shen, M. Kianinia, C. Bradac, I. Aharonovich, M. J. Ford, and P. Piecuch, Photoluminescence, photophysics, and photochemistry of the V_B^- defect in hexagonal boron nitride, *Phys. Rev. B* **102**, 144105 (2020).
- [11] F. Libbi, P. M. M. C. de Melo, Z. Zanolli, M. J. Verstraete, and N. Marzari, Phonon-assisted luminescence in defect centers from many-body perturbation theory, *Phys. Rev. Lett.* **128**, 167401 (2022).
- [12] C. Qian, V. Villafañe, M. Schalk, G. V. Astakhov, U. Kentsch, M. Helm, P. Soubelet, N. P. Wilson, R. Rizzato, S. Mohr, A. W. Holleitner, D. B. Bucher, A. V. Stier, and J. J. Finley, Unveiling the zero-phonon line of the boron vacancy center by cavity-enhanced emission, *Nano Lett.* **22**, 5137 (2022).
- [13] S. Kim, J. E. Fröch, J. Christian, M. Straw, J. Bishop, D. Totonjian, K. Watanabe, T. Taniguchi, M. Toth, and I. Aharonovich, Photonic crystal cavities from hexagonal boron nitride, *Nat. Commun.* **9**, 2623 (2018).
- [14] J. E. Fröch, S. Kim, N. Mendelson, M. Kianinia, M. Toth, and I. Aharonovich, Coupling Hexagonal Boron Nitride Quantum Emitters to Photonic Crystal Cavities, *ACS Nano* **14**, 7085 (2020).
- [15] C. Qian, V. Villafañe, P. Soubelet, A. Hötger, T. Taniguchi, K. Watanabe, N. P. Wilson, A. V. Stier, A. W. Holleitner, and J. J. Finley, Nonlocal exciton-photon interactions in hybrid high- q beam nanocavities with encapsulated mos_2 monolayers, *Phys. Rev. Lett.* **128**, 237403 (2022).
- [16] N. Mendelson, M. Doherty, M. Toth, I. Aharonovich, and T. T. Tran, Strain engineering of quantum emitters in hexagonal boron nitride (2019), [arXiv:1911.08072](https://arxiv.org/abs/1911.08072).
- [17] M. Autore, P. Li, I. Dolado, F. J. Alfaro-Mozaz, R. Esteban, A. Atxabal, F. Casanova, L. E. Hueso, P. Alonso-González, J. Aizpurua, A. Y. Nikitin, S. Vélez, and R. Hillenbrand, Boron nitride nanoresonators for phonon-enhanced molecular vibrational spectroscopy at the strong coupling limit, *Light: Sci. Appl.* **7**, 17172 (2018).
- [18] Y. Wang, J. Lee, X.-Q. Zheng, Y. Xie, and P. X.-L. Feng, Hexagonal boron nitride phononic crystal waveguides, *ACS Photonics* **6**, 3225 (2019).
- [19] M. K. Zalalutdinov, J. T. Robinson, J. J. Fonseca, S. W. LaGasse, T. Pandey, L. R. Lindsay, T. L. Reinecke, D. M. Photiadis, J. C. Culbertson, C. D. Cress, and B. H. Houston, Acoustic cavities in 2d heterostructures, *Nat. Commun.* **12**, 3267 (2021).
- [20] T. Yang, N. Mendelson, C. Li, A. Gottscholl, J. Scott, M. Kianinia, V. Dyakonov, M. Toth, and I. Aharonovich, Spin defects in hexagonal boron nitride for strain sensing on nanopillar arrays, *Nanoscale* **14**, 5239 (2022).
- [21] M. Eichenfield, R. Camacho, J. Chan, K. J. Vahala, and O. Painter, A picogram- and nanometre-scale photonic-crystal optomechanical cavity, *Nature* **459**, 550 (2009).
- [22] M. Eichenfield, J. Chan, R. M. Camacho, K. J. Vahala, and O. Painter, Optomechanical crystals, *Nature* **462**, 78 (2009).
- [23] C. Qian, V. Villafañe, P. Soubelet, A. V. Stier, and J. J.

- Finley, Exciton coupling with cavity vibrational phonons and mos_2 lattice phonons in hybrid nanobeam cavities (2022), [arXiv:2204.04304](https://arxiv.org/abs/2204.04304).
- [24] M. Kianinia, S. White, J. E. Fröch, C. Bradac, and I. Aharonovich, Generation of spin defects in hexagonal boron nitride, *ACS Photonics* **7**, 2147 (2020).
- [25] N.-J. Guo, W. Liu, Z.-P. Li, Y.-Z. Yang, S. Yu, Y. Meng, Z.-A. Wang, X.-D. Zeng, F.-F. Yan, Q. Li, J.-F. Wang, J.-S. Xu, Y.-T. Wang, J.-S. Tang, C.-F. Li, and G.-C. Guo, Generation of spin defects by ion implantation in hexagonal boron nitride, *ACS Omega* **7**, 1733 (2022).
- [26] M. Aspelmeyer, T. J. Kippenberg, and F. Marquardt, Cavity optomechanics, *Rev. Mod. Phys.* **86**, 1391 (2014).
- [27] J. Zhou, J. Zheng, Z. Fang, P. Xu, and A. Majumdar, Ultra-low mode volume on-substrate silicon nanobeam cavity, *Opt. Express* **27**, 30692 (2019).
- [28] J. Guo and S. Gröblacher, Integrated optical-readout of a high-q mechanical out-of-plane mode (2022), [arXiv:2202.06336](https://arxiv.org/abs/2202.06336).
- [29] J. Yan, S. Goler, T. D. Rhone, M. Han, R. He, P. Kim, V. Pellegrini, and A. Pinczuk, Observation of magnetophonon resonance of dirac fermions in graphite, *Phys. Rev. Lett.* **105**, 227401 (2010).
- [30] C. Dong, Y. Wang, and H. Wang, Optomechanical interfaces for hybrid quantum networks, *Natl. Sci. Rev.* **2**, 510 (2015).
- [31] J. Vučković, Quantum optics and cavity qed with quantum dots in photonic crystals (Oxford University Press, Oxford, 2017) pp. 365–406.
- [32] J. Li, E. R. Glaser, C. Elias, G. Ye, D. Evans, L. Xue, S. Liu, G. Cassabois, B. Gil, P. Valvin, T. Peline, A. L. Yeats, R. He, B. Liu, and J. H. Edgar, Defect engineering of monoisotopic hexagonal boron nitride crystals via neutron transmutation doping, *Chem. Mater.* **33**, 9231 (2021).
- [33] G.-C. Shan, Z.-Q. Yin, C. H. Shek, and W. Huang, Single photon sources with single semiconductor quantum dots, *Front. of Phys.* **9**, 170 (2014).
- [34] R. Heitz, M. Veit, N. N. Ledentsov, A. Hoffmann, D. Bimberg, V. M. Ustinov, P. S. Kop'ev, and Z. I. Alferov, Energy relaxation by multiphonon processes in InAs/GaAs quantum dots, *Phys. Rev. B* **56**, 10435 (1997).
- [35] A. W. Achtstein, O. Marquardt, R. Scott, M. Ibrahim, T. Riedl, A. V. Prudnikau, A. Antanovich, N. Owschimikow, J. K. N. Lindner, M. Artemyev, and U. Woggon, Impact of shell growth on recombination dynamics and exciton-phonon interaction in CdSe-CdS core-shell nanoplatelets, *ACS Nano* **12**, 9476 (2018).
- [36] P. Merkl, C.-K. Yong, M. Liebich, I. Hofmeister, G. Berghäuser, E. Malic, and R. Huber, Proximity control of interlayer exciton-phonon hybridization in van der Waals heterostructures, *Nat. Commun.* **12**, 1719 (2021).
- [37] I. Iatsunskyi, G. Nowaczyk, S. Jurga, V. Fedorenko, M. Pavlenko, and V. Smyntyna, One and two-phonon Raman scattering from nanostructured silicon, *Optik* **126**, 1650 (2015).
- [38] R. T. Howie, I. B. Magdău, A. F. Goncharov, G. J. Ackland, and E. Gregoryanz, Phonon localization by mass disorder in dense hydrogen-deuterium binary alloy, *Phys. Rev. Lett.* **113**, 175501 (2014).
- [39] A. K. Arora, M. Rajalakshmi, T. R. Ravindran, and V. Sivasubramanian, Raman spectroscopy of optical phonon confinement in nanostructured materials, *J. Raman Spectrosc.* **38**, 604 (2007).
- [40] V. I. Korepanov, Localized phonons in Raman spectra of nanoparticles and disordered media, *J. Raman Spectrosc.* **51**, 881 (2020).
- [41] G. Grosso, H. Moon, C. J. Ciccarino, J. Flick, N. Mendelson, L. Mennel, M. Toth, I. Aharonovich, P. Narang, and D. R. Englund, Low-temperature electron-phonon interaction of quantum emitters in hexagonal boron nitride, *ACS Photonics* **7**, 1410 (2020).
- [42] D. Hoch, X. Yao, and M. Poot, Geometric tuning of stress in pre-displaced silicon nitride resonators, *Nano Lett.* **22**, 4013 (2022).
- [43] H. Xie, S. Jiang, D. A. Rhodes, J. C. Hone, J. Shan, and K. F. Mak, Tunable exciton-optomechanical coupling in suspended monolayer MoSe_2 , *Nano Lett.* **21**, 2538 (2021).
- [44] M. Montinaro, G. Wüst, M. Munsch, Y. Fontana, E. Russo-Averchi, M. Heiss, A. Fontcuberta i Morral, R. J. Warburton, and M. Poggio, Quantum dot optomechanics in a fully self-assembled nanowire, *Nano Lett.* **14**, 4454 (2014).

Supplemental Material for Emitter-Optomechanical Interaction in high-Q hBN Nanocavities

Chenjiang Qian,^{1,*} Viviana Villafañe,¹ Martin Schalk,¹ Georgy V. Astakhov,² Ulrich Kentsch,² Manfred Helm,² Alexander Hötger,¹ Pedro Soubelet,¹ Alexander W. Holleitner,¹ Andreas V. Stier,¹ and Jonathan J. Finley^{1,†}

¹Walter Schottky Institut and Physik Department,

Technische Universität München, Am Coulombwall 4, 85748 Garching, Germany

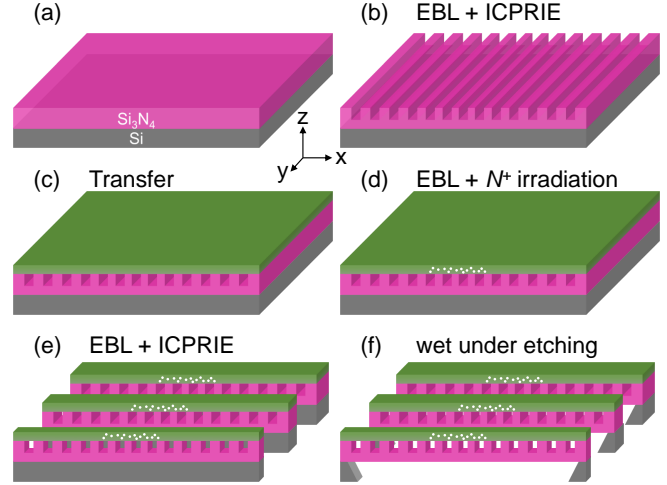
²Helmholtz-Zentrum Dresden-Rossendorf, Institute of Ion Beam Physics and Materials Research, 01328 Dresden, Germany

CONTENTS

I. Introduction	1
II. Methods	1
A. Sample Fabrication	1
B. Measurement Setup	2
C. Fitting Methods	2
III. V_B^- Induced Optical Bistability	4
A. Theory	4
B. Power Dependence	5
C. Control Experiments	5
IV. Vibration Controlled V_B^- Emissions	6
A. Control Experiments to Exclude Other Possibilities	6
B. Control Experiments to Identify Raman Peaks	6
C. Green Labelled Phonons	7
D. Other Minor Effects of V_B^- Phonons	7
E. Superposition of Cavity Vibrations	8
V. Resonant Excitation: Methods and Control Experiments	10
VI. Anticrossing between V_B^- Phonons	10
VII. Summary and Outlook	11
References	11

I. INTRODUCTION

In the main paper, we discuss and demonstrate the emitter-induced optomechanics and the cavity-induced control of phonon-assisted V_B^- emission. Here we present supplemental materials for this emitter-optomechanical interaction. In Sec. II, we introduce the methods used in this work, including the sample fabrication, the measurement setup and the fitting of experimental data. In Sec. III-VI, we present additional discussions for each



SFig. 1. Fabrication processes. (a) $\text{Si}_3\text{N}_4/\text{Si}$ substrate. (b) EBL and ICPRIE to fabricate periodic nanotrenches. (c) Transfer the hBN flake on top of the pre-etched Si_3N_4 . (d) Generate V_B^- site-selectively. (e) EBL and ICPRIE to divide the nanobeams. (f) Wet etching to remove the bottom Si.

experiment, including the control experiment to exclude other possibilities, the brief theory reproduced from reference papers and other experimental phenomena which are not the major focus of this work. The supplemental material further strengthens the conclusions of emitter-optomechanical interaction, and indicate potential future investigations on the hBN emitters and their applications in the cQED system.

II. METHODS

A. Sample Fabrication

The hBN/ Si_3N_4 hybrid nanobeam cavity is fabricated through e-beam lithography (EBL), inductively coupled plasma reactive ion etching (ICPRIE), viscoelastic dry transfer [1] and wet under etching. All of them are common technologies widely applied in nanocavities and 2D semiconductors. The fabrication processes of Sample-A are schematically depicted in SFig. 1. Firstly, we prepare Si substrate with 200nm Si_3N_4 grown by low pressure chemical vapor deposition (LPCVD) on top, as shown in SFig. 1(a). Then we use EBL and ICPRIE

* chenjiang.qian@wsi.tum.de

† finley@wsi.tum.de

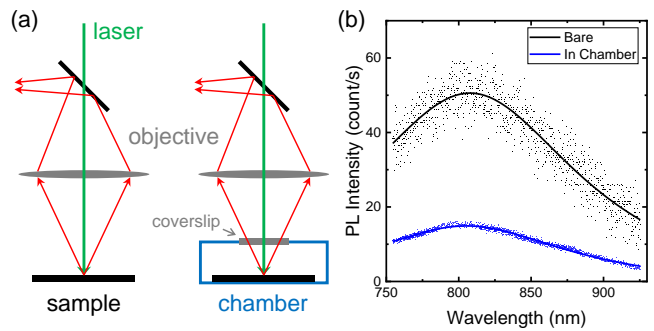
to etch the periodic nanotrenches in Si_3N_4 , as shown in SFig. 1(b). We chirp the periodicity of nanotrenches at the center to create photonic bandgap confinement. After the first etching, we transfer the hBN flake with a thickness ~ 100 nm on top of the pre-etched Si_3N_4 , as shown in SFig. 1(c). Then we cover the hBN flake by the resist mask and use EBL to pattern a window at the cavity center positions where we want to create V_B^- centers, as shown in SFig. 1(d). In this step the resist has the thickness > 600 nm to protect the hBN under the resist mask [2]. Finally, we use EBL and ICPRIE to divide the nanobeams as shown in SFig. 1(e), following by the wet etching to remove the bottom Si as shown in SFig. 1(f). The fabrication processes of Sample-B are generally the same. The only difference is that the V_B^- centers are not created site-selectively like in SFig. 1(d), but rather homogeneously in the whole hBN flake (without any resist mask) after all fabrication processes.

In our nanocavity, the hBN is not perforated and only etched at two sidewalls of the nanobeam. This optimization retains the *pristine* quality of 2D semiconductors and improves the Q-factor to $> 10^4$, at least one order of magnitude higher compared to previous 2D-material-based cavities. Fabrication details such as the e-beam dose, the gas for ICPRIE, etc. along with the calculation of cavity modes have been reported in our previous works [3–5].

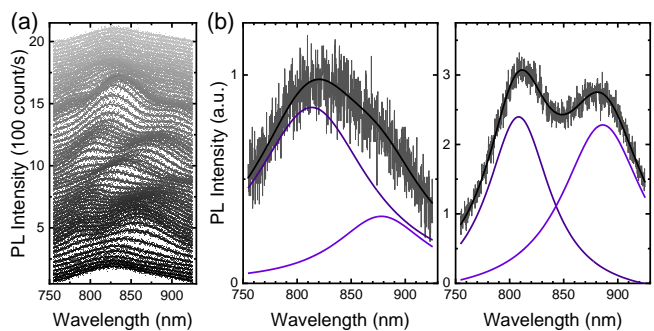
B. Measurement Setup

The samples are measured by a confocal micro-PL system. The objective with a magnification of 100 and a NA of 0.75 is used to focus the laser into a spot with the size $\sim 1 \mu\text{m}^2$ on the sample. The resonant excitation of cavity photons presented in Fig. 4 in the main paper is carried out with a tunable narrow-linewidth cw-laser. Other photoluminescence (PL) and Raman spectra are carried out with a 532nm cw-laser. The sample is mounted on a three-dimensional xyz nanopositioner for the position-dependent measurement. The PL and Raman spectra of V_B^- centers (e.g., Fig. 2-5 in the main paper) are collected by a matrix array Si CCD detector in a spectrometer, with the focal length of 0.55 m and the grating of 300 grooves per mm. The PL spectra of cavity photons (e.g., Fig. 1 in the main paper) are collected by the same detector and spectrometer but with the grating of 1200 grooves per mm.

In this work, the sample is measured at room temperature in the air, since we find the coverslip of our chamber will suppress and deform the signals, particularly at the wavelength over 800 nm. The confocal setup is schematically depicted in SFig. 2(a). For a high NA objective, the medium lying coverslip will critically affect the aplanatic and sine conditions, thereby introduces the spherical and chromatic aberrations [6, 7]. As a result, signals are suppressed when the sample is measured in chamber, shown by the comparison in SFig. 2(b). Moreover, we



SFig. 2. (a) Schematic of the confocal micro-PL setup, with the sample (left) bare in the air and (right) in the chamber. (b) Comparison of PL spectra measured at the same position with and without the coverslip, excited with the same laser power of $264 \mu\text{W}$.



SFig. 3. (a) PL spectra corresponding to Fig. 5(c) in the main paper. Peaks are very distinguishable. (b) Two fitting examples.

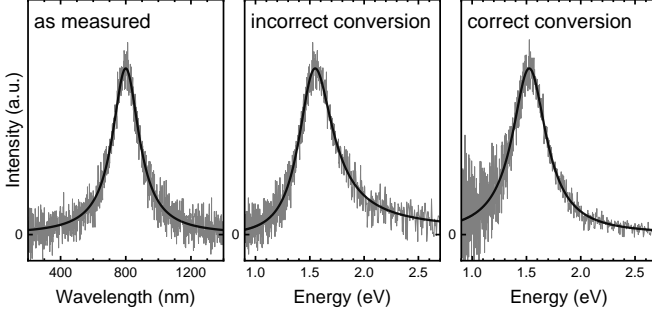
find this suppression increases with the wavelength, by $\sim 25\%$ from 800 to 920 nm. For PL signals of a sharp peak, such suppression will only decrease the counts and rarely affect the lineshape. But for the broad V_B^- emission shown in SFig. 2(b), the line shape will be affected by the non-uniform suppression. Therefore, we carry out the measurement in the air to collect the pure signals and avoid potential errors.

C. Fitting Methods

The PL peaks in spectra are very distinguishable. Indeed, the shifting of peaks can be clearly observed and traced even without fittings, e.g. datasets in Fig. 3 in the main paper and SFig. 3(a) here. Nevertheless, we still use multi-Lorentz fittings to improve the accuracy of extract dataset. Two examples are presented in SFig. 3(b). As shown, the fitting results are in good agreement with the raw data.

In this work, we fit the PL spectra in wavelength dimension for the accuracy. The PL spectrum is defined by the energy density distribution, as

$$\Delta E = f(\lambda) \Delta \lambda = g(\omega) \Delta \omega \quad (1)$$



SFig. 4. Comparison of the spectra as measured, incorrectly converted, and correctly converted. Black line is the standard Lorentz signal. Gray line is the presumptive data in measurement by adding a normal distributed noise.

where ΔE is the energy of photons in the differential wavelength range $\Delta\lambda$ or energy range $\Delta\omega$. The raw data collected by the spectrometer is $f(\lambda)$ at the wavelength λ dimension with equispaced points which means a constant $\Delta\lambda$. When converting the spectrum to the energy ω dimension, theoretically we cannot directly change the x-axis unit since $g(\omega) \neq f(hc_0/\omega)$, but

$$\begin{aligned} g(\omega) &= f(\lambda) \frac{\Delta\lambda}{\Delta\omega} \\ &= f\left(\frac{hc_0}{\omega}\right) \frac{hc_0}{\omega^2} \end{aligned} \quad (2)$$

where h is the Planck constant and c_0 is the vacuum light speed. For example, after converting the standard Lorentz peak with intensity A , peak wavelength λ_C and linewidth γ_λ

$$f(\lambda) = \frac{A}{\pi} \frac{\gamma_\lambda/2}{(\lambda - \lambda_c)^2 + (\gamma_\lambda/2)^2} \quad (3)$$

by Eq. (2), the spectra in the energy dimension still has the standard Lorentz shape

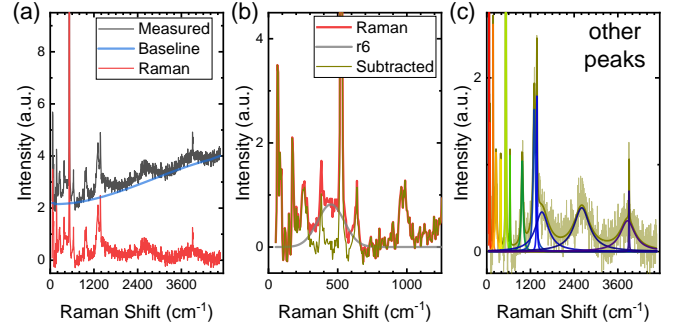
$$\begin{aligned} g(\omega) &= \frac{A}{\pi} \frac{\gamma_\lambda/2}{(hc_0/\omega - \lambda_c)^2 + (\gamma_\lambda/2)^2} \frac{hc_0}{\omega^2} \\ &= \frac{A}{\pi} \frac{\gamma_\omega/2}{(\omega - \omega_c)^2 + (\gamma_\omega/2)^2} \end{aligned} \quad (4)$$

with the peak energy ω_C and linewidth γ_ω as

$$\begin{aligned} \omega_c &= \frac{hc_0}{\lambda_c} \frac{1}{1 + \beta^2} \\ \gamma_\omega &= \frac{hc_0\gamma_\lambda}{\lambda_c^2} \frac{1}{1 + \beta^2} \\ \beta &= \frac{\gamma_\lambda}{2\lambda_c} = \frac{\gamma_\omega}{2\omega_c} \end{aligned} \quad (5)$$

. In contrast, if we incorrectly convert without the term $\Delta\lambda/\Delta\omega$ in Eq. (2), the result $f(hc_0/\omega)$ is not the Lorentz shape.

However, the conversion in Eq. (2) is only theoretically feasible, limited by the experimental noises. To straightforwardly clarify this point, we plot one example of the

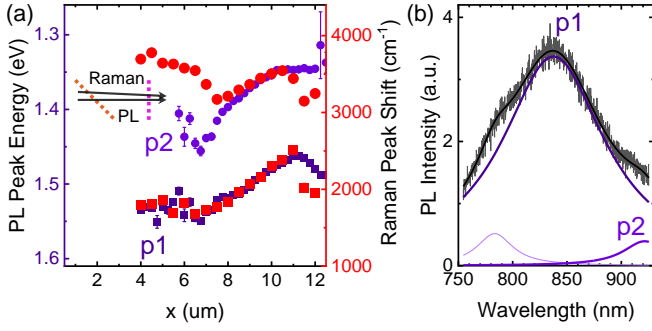


SFig. 5. (a) Raman spectrum (red) is extracted by subtracting the measured spectrum (gray) with the emission baseline (blue). (b) Peak r6 overlaps to many other peaks. Thus, we first subtract the Raman spectrum with a Gaussian-shape peak r6 (gray). Other peaks are then extracted by the multi-Lorentz fitting in (c).

Lorentz signal with $\lambda_C = 800$ nm and $\gamma_\lambda = 200$ nm in SFig. 4. We add a noise with the normal distribution to simulate the experimental noises, and the presumptive data in measurement is depicted by the gray line. As shown, after the incorrect conversion without the term $\Delta\lambda/\Delta\omega$, the peak in the energy dimension is deformed and not Lorentzian. Although the correct conversion by Eq. (2) retains the Lorentz lineshape in the energy dimension, the noise of data point significantly increases as ω decreases. Such non-uniform noise of data points makes the further analysis difficult. Generally, for a narrow PL peak either the incorrect or correct conversion (without or with $\Delta\lambda/\Delta\omega$) works, because $\Delta\lambda/\Delta\omega$ is approximately constant within a narrow range. But for broad PL peaks, the inaccurate deformation in incorrect conversion and the non-uniform noise in correct conversion both increase as the peak linewidth becomes broader (larger β in Eq. (5)) thus are both infeasible. Therefore, we use multi Lorentz peaks to fit the broad V_B^- emission in wavelength dimension (e.g. SFig. 3), and change the fitting results to energy dimension when necessary.

Above discussions are based on the theoretical definition of spectrum in Eq. (1) and the correct collection of $f(\lambda)$ by the spectrometer. One might wonder that the actual performance of the spectrometer and detector might differ to the expectation, e.g. Si CCD usually has low efficiency for the wavelength over 1000 nm, limiting the accuracy of Eq. (1). We mainly focus on the spectra with wavelength below 950 nm to avoid the inaccuracy from Si CCD detector. In addition, we note that the PL peak shift such as those shown in SFig. 3 are very distinguishable. Even if some inaccuracies are introduced by the fitting method, they will not affect the conclusions presented in the main paper.

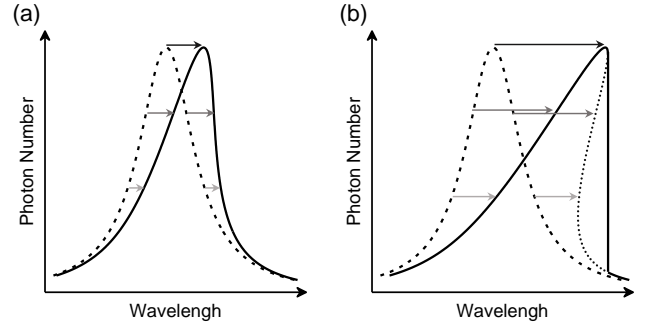
The measured spectra around the wavelength of excitation laser, e.g. the gray line in SFig. 5(a), consist of both Raman and PL signals superimposed. As a common method, we first draw the emission baseline based on the peak foots of Raman signals, and then extract the Raman



SFig. 6. (a) Energies of PL and Raman peaks corresponding to Fig. 3 in the main paper. Inset depicts the potential misalignments between the trace in PL and Raman maps. The orange and magenta dashed lines correspond to the boundaries between different regions (Fig. 2(b) in the main paper). (b) Fitting of PL spectrum at $x = 12 \mu\text{m}$. Fitting of p1 is accurate while that of p2 is limited by the measurement.

spectrum by subtracting the emission baseline from the measured data, such as the example in SFig. 5(a). In the Raman spectra, the broad peak of localized phonon r6 overlaps with many other peaks. Thereby, it is difficult to fit all overlapped peaks together. To separate these peaks, we first extract peak r6 by a Gaussian base peak as shown in SFig. 5(b). Then other peaks are fitted by multi Lorentz peaks as shown in SFig. 5(c). This fitting method might introduce some inaccuracy to the peak r6. However, as shown in Fig. 2(c) in the main paper and SFig. 5(b) here, peak r6 and other nearby peaks are quite distinguishable, thereby the inaccuracy is small. Moreover, as discussed in the main paper, the V_B^- emission wavelengths mainly depends on the multi-phonon states of localized phonons r12,13. Thus, even if some minor inaccuracy exists in the fitting of r6, our conclusions will not be affected. In addition, we note that for the broad localized phonons in $1400 - 4000 \text{ cm}^{-1}$, such as the three in SFig. 5(c), Lorentz and Gaussian fitting give the same peak energy since these peaks are distinguishable and do not overlap with other peaks. Therefore, the inaccuracy from the fitting methods of PL and Raman spectra has little impact on the conclusions in this work.

We note that due to the experimental limitation, the traces in PL and Raman map for comparison, e.g., Fig. 3 and 5 in the main paper, cannot match perfectly in spatial. SFig. 6 shows the energies of PL and Raman peaks corresponding to Fig. 3 in the main paper. As shown, the energy of PL peaks and localized phonons generally agree but exhibits minor misalignment. There are mainly two misalignments. Firstly, as shown in Fig. 5(a)(b) in the main paper, the PL and Raman map are measured separately, thereby, two maps have a small relative angle. Secondly, the integration time for each Raman spectrum is 10 times of that for each PL spectrum. For feasibility, we need to decrease the resolution of the Raman map. As shown in Fig. 5(a), we first use the step of $1 \mu\text{m}$ for a large $16 \times 16 \mu\text{m}$ Raman map, and then use the step of



SFig. 7. (a) The cavity mode peak is asymmetric due to the photon-phonon coupling. (b) The bistability occurs as the photon-phonon coupling further increases.

$0.5 \mu\text{m}$ for a small $8 \times 8 \mu\text{m}$ Raman map. In contrast, we use the step of $0.25 \mu\text{m}$ for the PL map. The different resolution means an unavoidable translational misalignment. These two misalignments are schematically shown in the inset in SFig. 6(a).

Meanwhile, the fitting accuracy of PL peaks at long wavelength is limited by the measurement. The PL spectrum at $x = 12 \mu\text{m}$ in SFig. 6(a) is presented in (b) along with the multi-Lorentz fitting. As shown, the fitting of PL peak p1 is accurate, but the fitting accuracy of p2 is limited since part of peak p2 is outside the measurement range. We note that even if we increase the measurement range, e.g. installing a grating of 150 grooves per mm, the fitting accuracy at long wavelength will still be limited by the decreasing efficiency off Si CCD detector. As a result shown in SFig. 6(a), the fitted energy of PL peak p1 quantitatively tracks the shift of the localized phonon, whilst that of p2 only qualitatively tracks. This is one of the reasons why we mainly focus on the PL peak p1 when later discussing the superposition of vibronic modes in SFig. 18 in Sec. IV E.

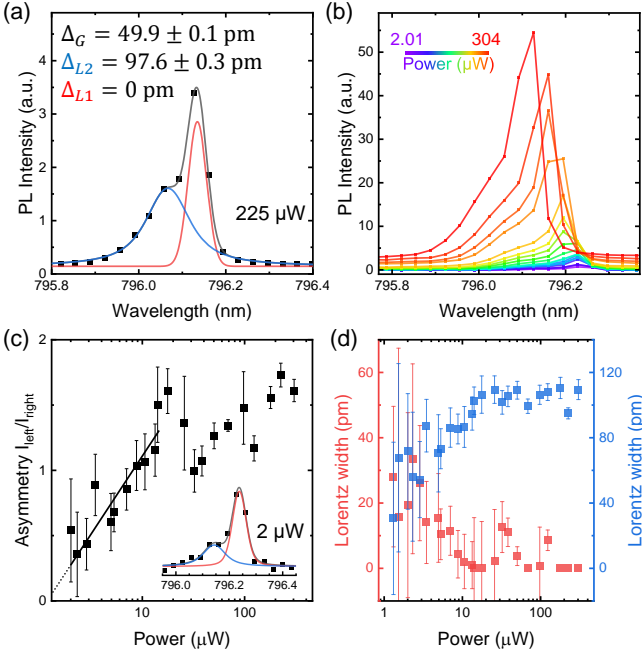
III. V_B^- INDUCED OPTICAL BISTABILITY

A. Theory

The optical bistability is a well-known optomechanical phenomenon originating from the photon-phonon coupling [8–10]. Without the photon-phonon coupling, the spectral density of cavity photons is well described by a Lorentz lineshape given by

$$\pi D_C(\omega) = (\gamma_C/2)/[(\omega - \omega_C)^2 + (\gamma_C/2)^2] \quad (6)$$

where ω_C and γ_C are the energy and decay rate of cavity photons [11]. An example is shown by the dashed lines in SFig. 7(a)(b). Considering the photon-phonon coupling with the phonon energy ω_p and the coupling strength g_p to a single photon, the optical resonance will be red shifted by an amount of $8g_p^2 N(\omega)/\omega_p$. $N(\omega)$ is the photon population proportional to $D_C(\omega)$. Therefore, as



SFig. 8. (a) The bi-Voigt fitting of one PL peak of cavity photons. (b) The power-dependent PL spectra. (c) The ratio between the intensity of two Voigt peaks, as a quantitation of the asymmetry. (d) The Lorentz width of the Voigt peaks, as a quantitation of the perpendicularity in the line shape.

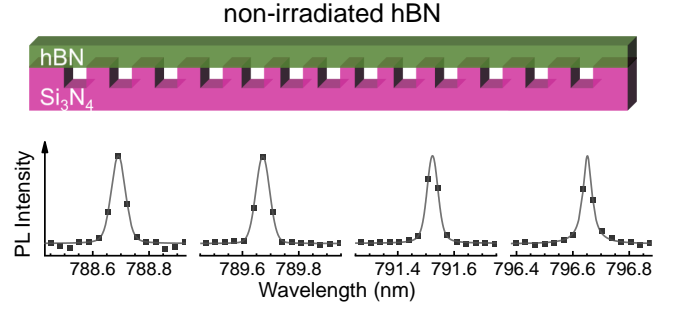
shown in SFig. 7(a)(b), more photons at the peak energy result in larger redshift induced from the photon-phonon coupling. This non-uniform energy shift results in the asymmetric peak lineshape reported in the main paper. Moreover, when the total population of photons N larger than the threshold value as [8]

$$N > \frac{\omega_p \gamma_C}{6\sqrt{3}g_p^2} \quad (7)$$

the peak shape is strongly deformed such as shown in SFig. 7(b). Such case with the perpendicular line shape at long wavelength side is the well-known optical bistability [8–10].

B. Power Dependence

Generally, as the excitation laser power increases, the asymmetry in the lineshape of cavity photons will increase since the photon-phonon coupling increases with the population of photons and phonons. For passive cavity without emitters, the peak wavelength should continuously red shift as the photon-phonon coupling increases [9, 10]. However, in our active cavities with V_B^- centers, the situation is complex. Firstly, the PL spectrum is broadened by the measurement setup by the convolution to a Gaussian window function [12, 13]. This broadening decreases the resolution and distinguishability of the PL spectra, as shown in SFig. 8(a). Secondly, in active



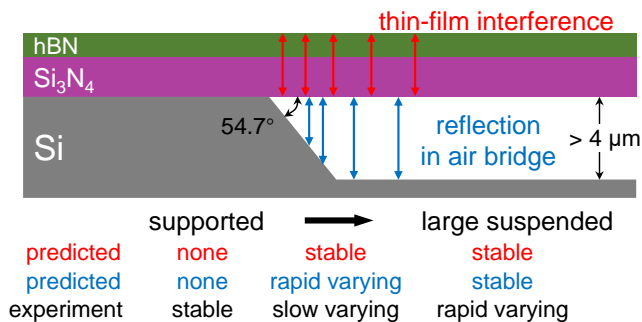
SFig. 9. Control experiments with non-irradiated hBN. No asymmetry is observed in the PL peak of cavity photons.

cavities there exist multiple factors contributing to the power-dependent energy shift of cavity photons, e.g., the laser-induced oxidation [14] and the pump-induced dephasing of cavity-emitter coupling [12, 15]. Thus, the peak wavelength will not simply red shift as observed for passive cavities. Indeed, blue shift is observed in our cavities with the increasing power, as shown in SFig. 8(b).

Despite these limitations, we still observe the photon-phonon coupling increasing with the laser power. We use two Voigt peaks, which is the convolution of Lorentz and Gaussian peak, to fit the PL peak of cavity photons as presented in SFig. 8(a). We note that such two peaks have no general physical meanings but provide a quantitation to describe the asymmetry and perpendicularity of the lineshape. The Gaussian width is set the same for the two Voigt peaks, and the fitting result in SFig. 8(a) shows this width $\Delta_G = 49.9 \pm 0.1$ pm. This value is consistent to the resolution 50 pm of our spectrometer, thereby, we fix $\Delta_G = 50$ pm in the fitting of other PL peaks. We use the ratio between the intensity of two Voigt peaks as the quantitation of asymmetry, and the results are presented in SFig. 8(c). As shown, the asymmetry generally increases with the laser power, and indicates a threshold power for the asymmetric lineshape of 9 ± 2 μ W. Moreover, the Lorentz width Δ_L of the Voigt peak describes the actual lineshape after deconvoluting the spectrometer broadening. Smaller Δ_L means more perpendicular lineshape. The Lorentz width of two Voigt peaks are presented in SFig. 8(d). As shown, when the power exceeds the threshold value of 10 μ W, Δ_L of the right peak (red) becomes zero, corresponding to the perpendicular lineshape in the optical bistability (SFig. 7(b)). Therefore, we clearly observe the photon-phonon coupling increasing with the laser power [9, 10], despite our active cavity is not completely same to the passive cavities.

C. Control Experiments

We carry out control experiments on the cavities with non-irradiated hBN to reveal the significant role of V_B^- in the photon-phonon coupling. SFig. 9 presents the spectra measured from four cavities, where the cavity mode



SFig. 10. Excluding air-bridge reflection and thin-film interference. As shown, the predicted position dependence of two effects in suspended structures can neither match the experimental observations.

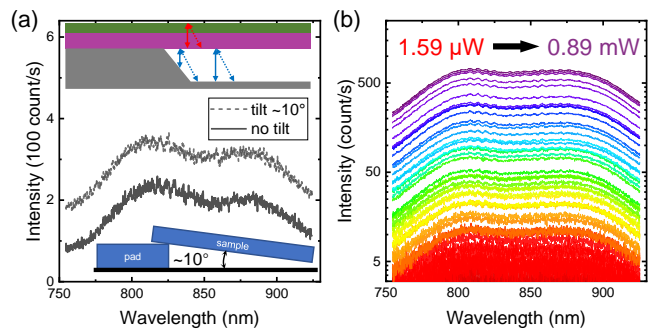
should be excited by some natural defects in hBN and Si_3N_4 . As shown, little asymmetry is observed. The asymmetry is also not observed for similar nanobeam cavities when the embedded emitter is free or localized excitons in MoS_2 monolayers [3]. Therefore, we conclude that the phonons involved in the photon-phonon coupling are from the V_B^- emission.

IV. VIBRATION CONTROLLED V_B^- EMISSIONS

A. Control Experiments to Exclude Other Possibilities

The position and geometry dependence in the PL and Raman spectra of V_B^- centers are well explained by the vibronic modes of freely suspended structures as discussed in the main paper. Here we present additional data and discussions to exclude other possible factors.

As shown in SFig. 10, the reflection in the underetched air bridge and the thin-film interference are two possible factors which might affect the PL spectra. The air bridge in sample-B is etched with 50% KOH solution, exhibiting a strong anisotropic etching which means $\langle 111 \rangle$ surface cannot be etched. Thus, the etching angle at the boundary of Si is always 54.7° . As a result, if the optical reflections in the air bridge plays the major role, their effect should vary rapidly at the boundary while be stable away the boundary. The thin-film interference depends on the thickness of hBN and Si_3N_4 , which have little variation in the whole sample. Therefore, the position dependence of these two effects can be predicted, as denoted in SFig. 10. However, as presented in Fig. 3 in the main paper, the position-dependent PL and Raman spectra vary slowly at the boundary while rapidly away the boundary. The prediction of two effects can neither match the experimental observations in the large suspended membrane. Indeed, due to the high concentration of KOH solution for the wet etching, some undissolved residuals left at the bottom surface of the air bridge such as shown in



SFig. 11. (a) Comparison of the PL spectra before/after tilting the sample. Little difference is observed. (b) Power-dependent PL spectra. No shifting or merging of peaks is observed.

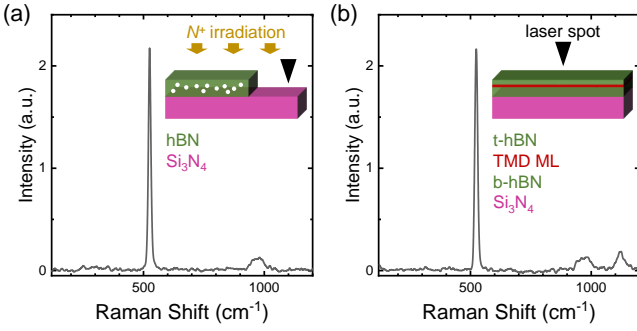
Fig. 2(b) in the main paper. With such rough surface, the reflection effect in the air bridge is expected to be neglectable.

In addition, the air bridge reflection and thin-film interference strongly depend on the tilting of the sample, as shown by the solid (before tilting) and dashed (after tilting) lines in the inset of SFig. 11(a). Particularly, the air bridge reflection would exhibit huge differences around the boundary, due to the 54.7° etching surface of Si. However, little difference is observed after we tilt the sample $\sim 10^\circ$. One comparison is shown in SFig. 11(a) for example. Moreover, if the multi PL peaks and anti-crossings in the suspended region are from the thin-film interference or other optical modes, we should observe the shift and merge of PL peaks as the pumping power increases [12, 15]. However, as shown by the power-dependent PL spectra in SFig. 11(b), no merging or shifting is observed. Considering the obvious contradictions between predictions and experimental results presented in SFig. 10 and 11, we exclude the optical effects of the air-bridge reflection and thin-film interference from our experimental observations.

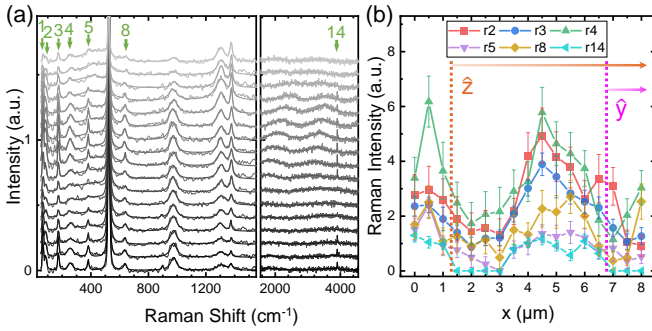
B. Control Experiments to Identify Raman Peaks

To identify the Raman peaks, we carry out the control experiments and typical results are presented in SFig. 12. The Raman spectrum measured at irradiated Si_3N_4 substrate without hBN is presented in SFig. 12(a). Only the peaks r7,9 from bulk Si_3N_4 are observed, indicating that even if some Si_3N_4 defects are created by the N^+ ions, these defects generate very few Raman signals in our measurement range. SFig. 12(b) presents a Raman spectrum measured at a non-irradiated hBN/ MoS_2 /hBN heterostructure standing on the Si_3N_4 substrate [5]. We identify the Raman peaks from V_B^- phonons by comparing these control experiments to the Raman spectra in Fig. 2(c) in the main paper.

The extended and highly localized phonons discussed in the main paper have been reported in previous works



SFig. 12. (a) Raman spectrum measured at Si_3N_4 substrate after N^+ ion irradiation (no hBN). (b) Raman spectrum measured at hBN/MoS₂/hBN heterostructure on Si_3N_4 substrate, without irradiation. Both are excited by 532nm cw-laser.

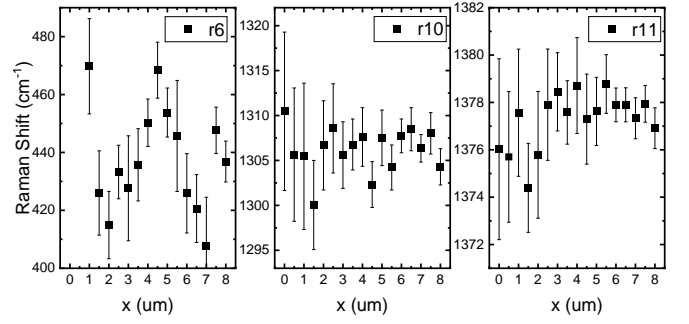


SFig. 13. Phonons r1-5,8,14 exhibit few direct relation to the V_B^- emission. (a) Position-dependent Raman spectra, extracted from the same trace as Fig. 3 in the main paper where the right panel is already presented. (b) The intensity variation of the green labelled phonons.

[16], therefore are surely from V_B^- . The green labelled phonons r1-5,8,14 are identified from V_B^- since they are observed in neither the irradiated Si_3N_4 nor the non-irradiated hBN as shown in SFig. 12. In addition, theoretical calculations show some V_B^- phonons within similar energy ranges [17], and similar phonons have been reported for nitrogen vacancies in hBN [18]. These references further support that the green labelled phonons are from V_B^- . Furthermore, as discussed next in Sec. IV C, the green labelled phonons exhibit few direct relation to the V_B^- emission, therefore, do not affect our conclusions in the main paper.

C. Green Labelled Phonons

The green labelled phonons r1-5,8,14 exhibit few direct relation to the V_B^- emissions, as shown by their position dependence presented in SFig. 13. The Raman spectra extracted from the same trace as Fig. 3 in the main paper are presented in SFig. 13(a), and the phonon intensities are presented in SFig. 13(b). The boundary between the non-underetched region and large suspended



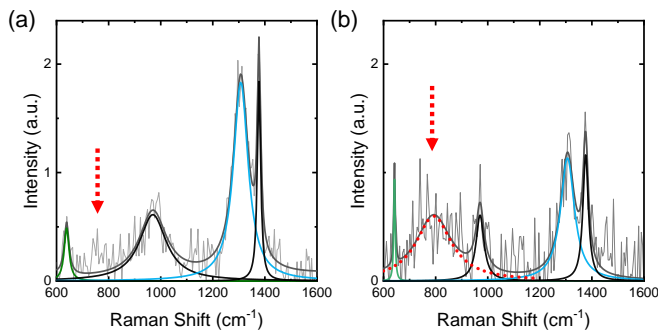
SFig. 14. Energy shift of phonons r6,10,11 extracted from SFig. 13(a).

membrane (orange dashed line), and the boundary between the large suspended membrane and nanobeam (magenta dashed line) are depicted in SFig. 13(b). As shown, all these green labelled phonons exhibit similar position dependence: a suppression at both two boundaries. Meanwhile, the phonons r1-5,8,14 have the energy 67, 86, 174, 256, 382, 638, 3909 cm^{-1} respectively, and no distinguishable energy shift is observed. Compared to the V_B^- emission presented in Fig. 3 in the main paper, we find few direct relation of these phonons to either the intensity or the wavelengths of the V_B^- emission.

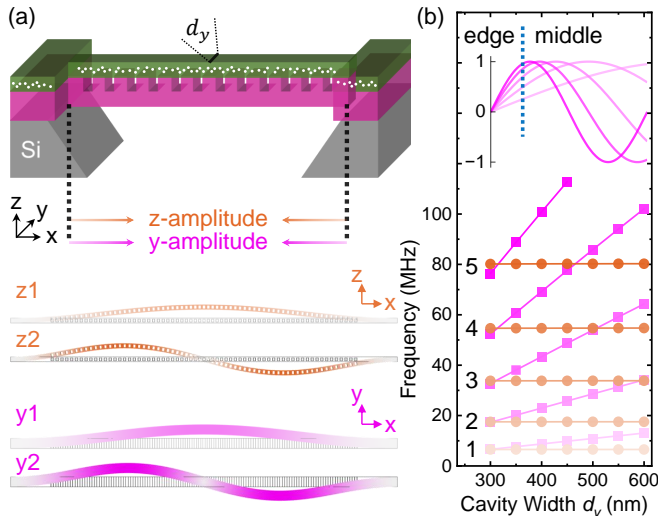
G. Grosso et al. [18] recently reported the study on the phonon processes of several nitrogen vacancies in hBN. They found that for nitrogen vacancies, phonons around 150 – 200 meV, which corresponds to the extended phonon r10 (162 meV) in this work, dominate the activation of emitters and determines the PL intensity. This is same to our observation for the V_B^- centers. Meanwhile, they also found the low-energy acoustic or out-plane optical phonons play fewer roles in emission of nitrogen vacancies [18]. We observe similar phenomena for the low-energy phonons r1-5. Since r8, 14 exhibit the same behavior to r1-5, we suggest all these green labelled phonons are the acoustic or out-plane optical phonons of V_B^- . We emphasize that, although no direct relation between the green labelled phonons and the V_B^- emission is observed, these phonons still exhibit position dependence as shown in SFig. 13. Thus, their roles in the emitter-optomechanical interaction might be minor but not zero. Specific details would be an interesting future topic.

D. Other Minor Effects of V_B^- Phonons

In this work, the ultra broad Raman peaks r6,12,13 are the only V_B^- phonons exhibiting distinguishable energy shift. The position-dependent energy shift of r12,13 are already discussed in the main paper. The shift of r6 is presented in SFig. 14. As discussed in Sec. II C, r6 is overlapped with many other peaks, introducing some inaccuracy in the fitting results. Nonetheless, the position-dependent energy shift is still clearly observed. For other



SFig. 15. Raman spectra measured at two positions in the suspended region. We can observe another broad peak around 800 cm^{-1} in some cases.



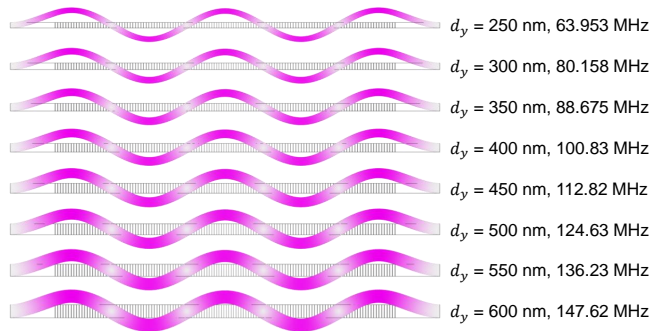
SFig. 16. (a) Schematic of the nanobeam cavity and the y_i and z_j vibronic modes. (b) Calculated vibration frequencies of modes y_1 -5 and z_1 -5. Insets show the vibration profile for modes y_1 -5.

phonons such as the extended V_B^- phonon r10 and bulk hBN phonon r11 presented in SFig. 14, there might be some vibration-induced energy shift. However, these energy shifts are very small, thereby we cannot distinguish them due to the low signal noise ratio (SNR).

Besides the Raman peaks r1-14, in some cases we could observe other minor peaks in the Raman spectra. For example, sometimes we could observe another broad peak around 800 cm^{-1} , as shown in SFig. 15, which might be another multi-phonon state of the localized phonon r6. However, the SNR of such peaks are very low, and they cannot always be observed in the measurement. Thereby, we do not further discuss these minor peaks.

E. Superposition of Cavity Vibrations

In the main paper, we discuss the case where the effects from y -/ z - vibronic modes can be separated by the

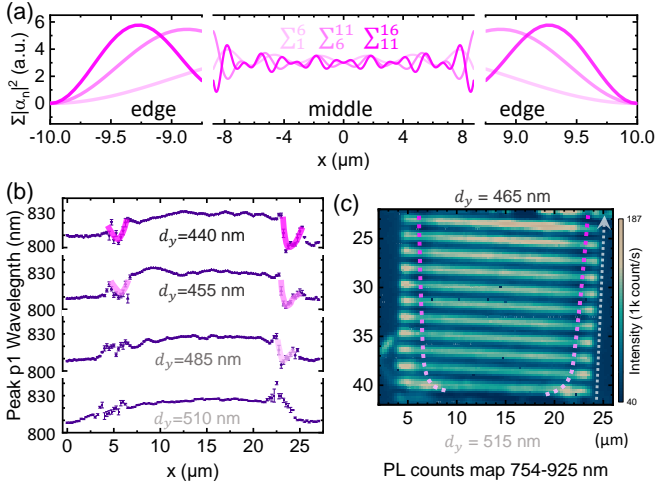


SFig. 17. Calculated y_5 mode for cavities with varying nanobeam width d_y .

comparison between the large suspended membrane and the nanobeam. In contrast, for the nanobeam cavities directly clamped to the non-underetched region (without the large suspended membrane) schematically illustrated in SFig. 16(a), the y -/ z - vibronic modes cannot be separated, and the nanobeam state of motion is described by the superposition of different modes. We calculate the nanobeam vibronic modes using the finite element method [5]. The y -/ z - vibronic modes are labelled according to the local harmonics (number of anti-nodes). Hereby, the modes are indexed in the figure as y_i and z_j where $i, j \in (1, 2, 3, \dots)$ respectively, such as the z_1 , z_2 , y_1 and y_2 modes plotted in SFig. 16(a).

We have nanobeam cavities with varying width d_y on the sample. The d_y -dependent frequency of y_i and z_j modes are presented in SFig. 16(b). As clearly observed from the results, the central result is that the frequency of all y_i modes strongly depends on d_y , while the frequency of all z_j modes rarely changes with d_y . As an example, we plot the y_5 mode of cavities with $d_y = 250 - 600 \text{ nm}$ in SFig. 17. This is due to that, the y - (z -) vibration frequencies of a nanobeam depend on the y - (z -) bending rigidities which is determined by the width of nanobeam in y (z) direction d_y (d_z) [19]. In our sample, d_z is fixed by the thickness of hBN and Si_3N_4 , whilst d_y varies between different nanobeam cavities. Therefore, d_y varies the frequency of y_i modes but not z_j modes. Such dependence means that for a given frequency, the harmonic i of corresponding y_i mode will increase as d_y decreases, whilst the harmonic j of corresponding z_j mode is constant. The different modes result in the different vibration amplitude. We plot the profile of y_i modes $i = 1 - 5$ in the inset of SFig. 16(b). As shown, at nanobeam edge the y -amplitude increases with increasing i (decreasing d_y), whilst at the middle region the y -amplitude is non-trivial.

We note that the optical and mechanical properties of hBN are not well known yet and strongly depend on the specific flake such as the local defect concentration [20]. In this work, we tentatively use the parameters of Si_3N_4 for the hBN, which means all materials are set to Si_3N_4 in the calculations, to achieve a numerical result. This might introduce differences between the calculation and experiment. However, we emphasize that



SFig. 18. (a) The sum amplitude of multiple y_i modes. \sum_1^6 , \sum_6^{11} and \sum_{11}^{16} are the simulation of a broad, medium and narrow cavity, respectively. (b) PL shift of p1 and (c) total PL intensity in nanobeam cavities, corresponding to the bottom part of the SEM image in Fig. 2(b) in the main paper. Magenta lines in (b)(c) denote the blue shift of p1 and the suppression of total PL intensity at nanobeam edges. These are both y -effects and increase as d_y decreases, agreeing perfectly to the theoretical predictions in (a).

the varying frequencies of y_i modes are due to the bending rigidity changes with the spatial extent in y -direction (d_y) [19]. In contrast, the bending rigidity in z -direction rarely changes, due to the spatial extent in z -direction (thickness of hBN and Si_3N_4) is same for all nanobeams. The geometric dependence of bending rigidity is the fundamental property in mechanics and does not rely on the parameters of specific materials. Therefore, although the absolute value of frequencies in the calculation might differ to the experiment, the key which means the different d_y dependence of y -/ z - modes, are always true.

Next, we use the simple trigonometric profiles

$$\alpha_i = \sin(i\pi(x/L + 1/2)) \quad (8)$$

to describe the eigenmodes and predict the superposition of multiple y_i modes. Here, L is the nanobeam length and $x \in (-L/2, L/2)$ is the position along the nanobeam relative to the center point [21]. We simulate the coupling effect of the superposition state to V_B^- by summing the amplitudes of multiple modes with random phase factors. Strictly, the summed coupling effect $a(x)$ should be

$$a(x) = \sum_f n(f) |g(f) \alpha_f(x)|^2 \quad (9)$$

where α_f is the vibration profile of mode y_i which has the frequency f , $n(f)$ is the Bose factor $n(f) = 1/[e^{hf/(k_B T)} - 1]$ where k_B is the Boltzmann constant, and $g(f)$ reflects the coupling strength to V_B^- . For a given f , the corresponding mode order i changes with the nanobeam width d_y . Meanwhile, $g(f)$ is an intrinsic

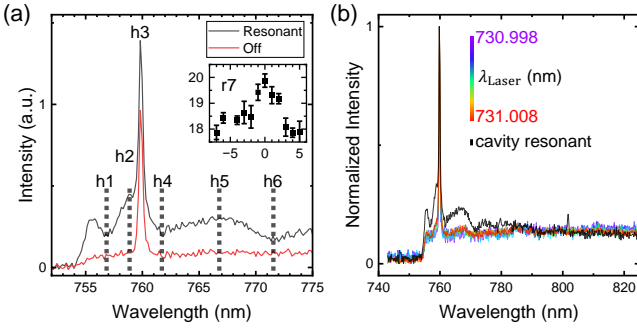
property of V_B^- and does not change with d_y . Theoretically we could predict the d_y dependence of the superposition based on Eq. (9).

However, $g(f)$ is difficult to get by either calculation or experiment. For a simple but qualitative example, here we calculate the superposition according to

$$a(x) = \sum_{i \in G} |\alpha_i(x)|^2 \quad (10)$$

where $i \in G$ means the y_i modes have the frequencies within the range G which couples to V_B^- . G is an intrinsic property of V_B^- , and the corresponding harmonics i within G changes with d_y . We assume that for a broad cavity with large d_y , $i \in G = 1 - 6$ thus the superposition (coupling) $a(x) = \sum_1^6$. Similarly, for a medium cavity $i \in G = 6 - 11$ and for a narrow cavity $i \in G = 11 - 16$. The three superpositions are presented in Fig. 18(a). As shown, $a(x)$ at nanobeam edges clearly increase as d_y decreases. This is due to the nanobeam edge $x = \pm L/2$ is the node of all modes, thus the sum of multiple y_i modes retains the d_y dependence of each mode discussed for the inset of SFig. 16. In contrast, in the middle region, the nodes of different modes are interlaced, thereby, the sum exhibits only minor variations. Therefore, based on SFig. 18(a) we can predict that as d_y decreases, the y -effects of V_B^- emission at nanobeam edges become stronger, but the V_B^- emission in the middle of the nanobeam exhibits little position or d_y dependence. Meanwhile, the z -effects of V_B^- emission is not affected by d_y .

The highly simplified approach Eq. (10) is not strictly equal to the correct approach Eq. (9). However, we can expect the results obtained by Eq. (9) would be qualitatively similar to the simple approach of Eq. (10), because the two fundamental properties, which means that the nanobeam edge is the node of all modes and the nodes of multiple modes are interlaced in the middle, are always correct and not affected by the simplicity of Eq. (10). Indeed, the theoretical predictions in SFig. 18(a) agree perfectly to the experimental observations as presented in Fig. 18(b)(c). As discussed for Fig. 3 in the main paper, the y -vibration blue shifts PL peak p1 and suppress the PL intensity. The "concave" blue shift of PL peak p1 in Fig. 18(b), corresponding to the "convex" y -amplitude predicted in Fig. 18(a), becomes significant as d_y decreases. Meanwhile, from edge to middle, the PL intensity is firstly enhanced (z -effect) and then suppressed (y -effect), resulting in the bright bar at nanobeam edges shown in Fig. 18(c). As d_y decreases, the bright bar becomes shorter, indicating stronger suppression from y -vibrations. Moreover, in contrast to these clear effects at nanobeam edges, the V_B^- emissions in the middle region are generally stable but with trivial variations. All these results are consistent to the predictions in Fig. 18(a). These perfect agreements of d_y dependence between theory and experiment further supports the conclusion of emitter-optomechanical interaction discussed in the main paper.

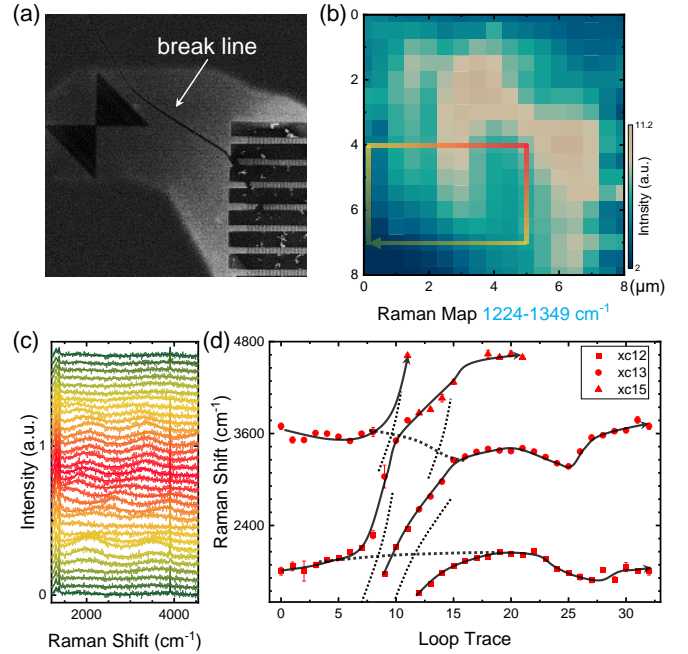


SFig. 19. (a) Comparison of the spectra at/off resonance and the method to extract peak heights. Inset is the peak height of the Si_3N_4 phonon r7. (b) Control experiments. Color lines are the normalized spectra measured in the large suspended membrane (no photonic mode), with the same laser tuned from 730.998 to 731.008 nm. Black line is the resonant spectra at cavity center for comparison.

Besides the vibration of the whole nanobeam presented in SFig. 18, our cavity also supports the confined vibronic modes at the cavity center with the frequency at GHz magnitude [5, 22]. In our previous work, we find that the MoS_2 exciton couples to both the beam and confined vibronic modes [5]. In contrast, in most cavities here, no particular variation of V_B^- emission wavelength or intensity is observed at the cavity center, as shown in Fig. 18(b)(c). This phenomenon indicates that V_B^- prefers to couple to MHz vibrations rather than GHz vibrations.

V. RESONANT EXCITATION: METHODS AND CONTROL EXPERIMENTS

In the resonant excitation of cavity photons presented in Fig. 4 in the main paper, we use a filter to cut the laser signal. The cutting can be clearly observed in the spectra. Since the Raman signals are close to the cut wavelength, they might also be affected by the filter more or less, making the subtracting and fitting of the spectra difficult. Therefore, we extract the peak height for brevity, as shown in SFig. 19(a). We directly extract the data points as denoted by h1-6. The peak height of V_B^- phonon r6 is calculated by $h_{r6} = h2 - h1$, and the peak height of r8 is calculated by $h_{r8} = h5 - (h4 + h6)/2$. These two heights are presented in Fig. 4 in the main paper. We note that for the peak at 766 nm (h5) in SFig. 19(a), the Raman shift 625 cm^{-1} agrees to the phonon r8 but the linewidth is broader. This might originate from the coupling effect to the cavity optomechanics, or the impact of another broad phonon discussed in SFig. 15. Whether which case it is, the major conclusion that V_B^- phonons are enhanced by the coupling to cavity photons, is not affected. This conclusion is strengthened by the control experiments presented in SFig. 19(b). We use the same tunable laser and measure the spectra at a



SFig. 20. (a) Left top part of the SEM image in Fig. 2(b) in the main paper. The large suspended membrane originates from a break line during the fabrication. (b) Raman map in Fig. 5(a) in the main paper. Raman spectra extracted from the color loop trace are in (c), and the corresponding fitting energy of localized phonons are in (d). Anticrossings between Raman peaks, similar to the anticrossings between PL peaks in Fig. 5(d) in the main paper.

position in the large suspended membrane. As expected, no resonant behavior is observed in the control experiment without the cavity photonic mode.

In addition, the peak height of Si_3N_4 phonon r7 calculated by $h_{r7} = h3 - h2$ is presented in the inset of SFig. 19(a). As shown, only $\sim 10\%$ enhancement at resonance is observed, revealing that the coupling of cavity photons to Si_3N_4 phonons are much weaker compared to that to V_B^- phonons. Moreover, compared to the enhancement of V_B^- phonons in Fig. 4 in the main paper, the enhancement of Si_3N_4 phonon is much more symmetric, indicating the cavity vibrations play limited roles here. This result further supports our conclusion of the vibration-mediated coupling between cavity photons and V_B^- phonons.

VI. ANTICROSSING BETWEEN V_B^- PHONONS

The large suspended membrane in the sample indeed originates from a break line during the fabrication, as shown in SFig. 20(a). The KOH solution etches the Si below the large suspended membrane in the wet under etching process through this break line created during the ICPRIE etching. The z-vibration has the maximum amplitude around the break line. As expected,

the corresponding total PL intensity and Raman intensity of phonon r10 are both strongest, as presented in Fig. 5(a)(b) in the main paper.

In addition, to avoid unexpected position dependence from the break line, the trace ① in Fig. 5(a)(b) which corresponds to Fig. 3, and the loop trace in Fig. 5(b) which corresponds to Fig. 5(d) in the main paper, both avoid this break line to make the conclusions convincing. Here we extract the Raman spectra from the loop trace in SFig. 20(b) (the break line avoided) and the results are presented in SFig. 20(c). The fitting energy of localized phonons are presented in SFig. 20(d). Similar to the PL peaks in Fig. 5(e) in the main paper, anticrossings are observed in the Raman spectra here, denoted by the dashed lines. These results further strengthen the consistency between Raman and PL spectra, and support our conclusion of the strong coupling between V_B^- phonon states from the Raman point of view.

VII. SUMMARY AND OUTLOOK

In this supplemental material, we present theoretical and experimental results to further strengthen our conclusions about the emitter-optomechanical interaction in the cavity- V_B^- system. We present the power-dependent asymmetry and perpendicularity of PL peaks in Sec. III to strengthen the emitter-induced cavity optomechanics. The cavity-induced control of phonon-assisted V_B^- emissions are strengthened by excluding other possibilities, carrying out control experiments and additional datasets as discussed in Sec. IV, V and VI. These results are consistent with each other, providing strong supports to the main paper.

In this work, we use a brief and fundamental model to describe the multipartite interplay between defect emis-

sion, defect phonons, cavity photons and cavity vibrations and well explain the emitter-optomechanical interaction. Meanwhile, we note that some specific details can be interesting future topics. E.g., besides the y-/z- vibrations, the nanobeam cavity also supports x-vibrations, rotate vibrations and cavity confined vibrations, which usually have much higher frequencies [5, 22]. Since V_B^- will interact with multiple vibrations, it would be an interesting topic to control the vibronic modes separately. Considering the zero-phonon line emission of V_B^- around 773 nm [4] and the first replica peak p1 around 805 nm in the non-underetched region, we could expect that peak p1 originates from the zero-phonon state by first absorbing an extended phonon r10 (1306 cm^{-1}) and then emit a highly localized phonon r12 (1800 cm^{-1}). The green labelled phonons also exhibit interaction effects with the vibrations, as discussed in Sec. IV C. These results indicate more specific details in the phonon-assisted emission dynamics of V_B^- , which are not well studied yet.

In addition, usually an emitter is either bright with the strong zero-phonon emission or dark due to the small or antisymmetric wavefunction overlap between electrons and holes. The unique phonon-assisted bright emission of V_B^- is the key to the emitter-optomechanical interaction, as discussed in this work. We suggest the hyperbolic dispersion [23] which provides strong confinement of phonons in hBN is a potential reason for this unique emission. Previous works reported that the hyperbolic can be controlled by nanostructures [24, 25] or even the simple suspending of hBN flakes [26]. Such controls are similar to the cavity-induced control of V_B^- centers here. We believe further investigations on the relationship between the phonon-assisted emission and the hyperbolic would help unveiling more unique emitters and extends the application of emitter-optomechanical interaction.

-
- [1] F. Pizzocchero, L. Gammelgaard, B. S. Jessen, J. M. Caridad, L. Wang, J. Hone, P. Bøggild, and T. J. Booth, The hot pick-up technique for batch assembly of van der Waals heterostructures, *Nat. Commun.* **7**, 11894 (2016).
 - [2] N.-J. Guo, W. Liu, Z.-P. Li, Y.-Z. Yang, S. Yu, Y. Meng, Z.-A. Wang, X.-D. Zeng, F.-F. Yan, Q. Li, J.-F. Wang, J.-S. Xu, Y.-T. Wang, J.-S. Tang, C.-F. Li, and G.-C. Guo, Generation of spin defects by ion implantation in hexagonal boron nitride, *ACS Omega* **7**, 1733 (2022).
 - [3] C. Qian, V. Villafañe, P. Soubelet, A. Hötger, T. Taniguchi, K. Watanabe, N. P. Wilson, A. V. Stier, A. W. Holleitner, and J. J. Finley, Nonlocal exciton-photon interactions in hybrid high- q beam nanocavities with encapsulated mos_2 monolayers, *Phys. Rev. Lett.* **128**, 237403 (2022).
 - [4] C. Qian, V. Villafañe, M. Schalk, G. V. Astakhov, U. Kentsch, M. Helm, P. Soubelet, N. P. Wilson, R. Rizzato, S. Mohr, A. W. Holleitner, D. B. Bucher, A. V. Stier, and J. J. Finley, Unveiling the zero-phonon line of the boron vacancy center by cavity-enhanced emission, *Nano Lett.* **22**, 5137 (2022).
 - [5] C. Qian, V. Villafañe, P. Soubelet, A. V. Stier, and J. J. Finley, Exciton coupling with cavity vibrational phonons and mos_2 lattice phonons in hybrid nanobeam cavities (2022), [arXiv:2204.04304](https://arxiv.org/abs/2204.04304).
 - [6] E. E. Diel, J. W. Lichtman, and D. S. Richardson, Tutorial: avoiding and correcting sample-induced spherical aberration artifacts in 3d fluorescence microscopy, *Nat. Protoc.* **15**, 2773 (2020).
 - [7] K. R. Spring and M. W. Davidson, **Spherical aberration from coverslip thickness variations**.
 - [8] M. Aspelmeyer, T. J. Kippenberg, and F. Marquardt, Cavity optomechanics, *Rev. Mod. Phys.* **86**, 1391 (2014).
 - [9] J. Zhou, J. Zheng, Z. Fang, P. Xu, and A. Majumdar, Ultra-low mode volume on-substrate silicon nanobeam cavity, *Opt. Express* **27**, 30692 (2019).
 - [10] J. Guo and S. Gröblacher, Integrated optical-readout of a high- q mechanical out-of-plane mode (2022), [arXiv:2202.06336](https://arxiv.org/abs/2202.06336).
 - [11] J. Vučković, Quantum optics and cavity qed with quan-

- tum dots in photonic crystals (Oxford University Press, Oxford, 2017) pp. 365–406.
- [12] M. Nomura, N. Kumagai, S. Iwamoto, Y. Ota, and Y. Arakawa, Laser oscillation in a strongly coupled single-quantum-dot–nanocavity system, *Nat. Phys.* **6**, 279 (2010).
- [13] J. Jimenez-Mier, Contribution of the instrument window function to the profile of autoionizing resonances, *J. Quant. Spectrosc. Radiat. Transfer* **51**, 741 (1994).
- [14] M. Tsuchiya, S. K. Sankaranarayanan, and S. Ramanathan, Photon-assisted oxidation and oxide thin film synthesis: A review, *Prog. Mater. Sci.* **54**, 981 (2009).
- [15] P. Yao, P. K. Pathak, E. Illes, S. Hughes, S. Münch, S. Reitzenstein, P. Franeck, A. Löffler, T. Heindel, S. Höfling, L. Worschech, and A. Forchel, Nonlinear photoluminescence spectra from a quantum-dot–cavity system: Interplay of pump-induced stimulated emission and anharmonic cavity qed, *Phys. Rev. B* **81**, 033309 (2010).
- [16] J. Li, E. R. Glaser, C. Elias, G. Ye, D. Evans, L. Xue, S. Liu, G. Cassabois, B. Gil, P. Valvin, T. Pelini, A. L. Yeats, R. He, B. Liu, and J. H. Edgar, Defect engineering of monoisotopic hexagonal boron nitride crystals via neutron transmutation doping, *Chem. Mater.* **33**, 9231 (2021).
- [17] J. R. Reimers, J. Shen, M. Kianinia, C. Bradac, I. Aharonovich, M. J. Ford, and P. Piecuch, Photoluminescence, photophysics, and photochemistry of the V_B^- defect in hexagonal boron nitride, *Phys. Rev. B* **102**, 144105 (2020).
- [18] G. Grosso, H. Moon, C. J. Ciccarino, J. Flick, N. Mendelson, L. Mennel, M. Toth, I. Aharonovich, P. Narang, and D. R. Englund, Low-temperature electron–phonon interaction of quantum emitters in hexagonal boron nitride, *ACS Photonics* **7**, 1410 (2020).
- [19] D. Hoch, X. Yao, and M. Poot, Geometric tuning of stress in predisplaced silicon nitride resonators, *Nano Lett.* **22**, 4013 (2022).
- [20] S. Thomas, K. M. Ajith, S. Chandra, and M. C. Valsakumar, Temperature dependent structural properties and bending rigidity of pristine and defective hexagonal boron nitride, *J. Phys.: Condens. Matter* **27**, 315302 (2015).
- [21] H. B. Khaniki, M. H. Ghayesh, R. Chin, and S. Husain, Nonlinear continuum mechanics of thick hyperelastic sandwich beams using various shear deformable beam theories, *Continuum Mech. Thermodyn.* **34**, 781 (2022).
- [22] M. Eichenfield, J. Chan, R. M. Camacho, K. J. Vahala, and O. Painter, Optomechanical crystals, *Nature* **462**, 78 (2009).
- [23] S.-A. Biehs, M. Tschikin, and P. Ben-Abdallah, Hyperbolic metamaterials as an analog of a blackbody in the near field, *Phys. Rev. Lett.* **109**, 104301 (2012).
- [24] J. D. Caldwell, A. V. Kretinin, Y. Chen, V. Giannini, M. M. Fogler, Y. Francescato, C. T. Ellis, J. G. Tischler, C. R. Woods, A. J. Giles, M. Hong, K. Watanabe, T. Taniguchi, S. A. Maier, and K. S. Novoselov, Sub-diffractive volume-confined polaritons in the natural hyperbolic material hexagonal boron nitride, *Nat. Commun.* **5**, 5221 (2014).
- [25] P. Pons-Valencia, F. J. Alfaro-Mozaz, M. M. Wiecha, V. Bielek, I. Dolado, S. Vélez, P. Li, P. Alonso-González, F. Casanova, L. E. Hueso, L. Martín-Moreno, R. Hillenbrand, and A. Y. Nikitin, Launching of hyperbolic phonon-polaritons in h-bn slabs by resonant metal plasmonic antennas, *Nat. Commun.* **10**, 3242 (2019).
- [26] S. Dai, J. Quan, G. Hu, C.-W. Qiu, T. H. Tao, X. Li, and A. Alù, Hyperbolic phonon polaritons in suspended hexagonal boron nitride, *Nano Lett.* **19**, 1009 (2019).